Final Report

for

Investigation of Dynamic Force/Vibration Transmission Characteristics of Four-Square Type Gear Durability Test Machines

NASA Grant Number

NAG3-2641

Grant Duration

August 1, 2001 to March 31 2002

Ahmet Kahraman

Principal Investigator

Department of Mechanical, Industrial and Manufacturing Engineering
The University of Toledo
Toledo, OH 43606

May, 2002

1. Motivation, Scope and Objectives

In this study, design requirements for a dynamically viable four-square type gear test machine are investigated. Variations of four-square type gear test machines have been in use for durability and dynamics testing of both parallel- and cross-axis gear set. The basic layout of these machines is illustrated in Figure 1. The test rig is formed by two gear pairs of the same reduction ratio, a test gear pair and a reaction gear pair, connected to each other through shafts of certain torsional flexibility to form an efficient, closed-loop system. A desired level of constant torque is input to the circuit through mechanical (a split coupling with a torque arm) or hydraulic (an hydraulic actuator) means. The system is then driven at any desired speed by a small DC motor.

The main task in hand is the isolation of the test gear pair from the reaction gear pair under dynamic conditions. Any disturbances originated at the reaction gear mesh might potentially travel to the test gearbox, altering the dynamic loading conditions of the test gear mesh, and hence, influencing the outcome of the durability or dynamics test. Therefore, a proper design of connecting structures becomes a major priority. Also equally important is the issue of how close the operating speed of the machine is to the resonant frequencies of the gear meshes.

This study focuses on a detailed analysis of the current NASA Glenn Research Center gear pitting test machine for evaluation of its resonance and vibration isolation characteristics. A number of these machines as the one illustrated in Figure 2 has been used over last 30 years to establish an extensive database regarding the influence of the gear materials, processes, surface treatments and lubricants on gear durability. This study is intended to guide an optimum design of next generation test machines for the most desirable dynamic characteristics. The scope of this study includes:

- a detailed vibration excitation analysis of NASA GRC gear durability test machine,
- development of dynamic models for evaluation of the current test machine for resonances and force/vibration transmission and isolation, and
- determination mechanical requirements for the connecting shaft structures and inertias for optimal dynamic behavior within the speed and torque ranges of operation.

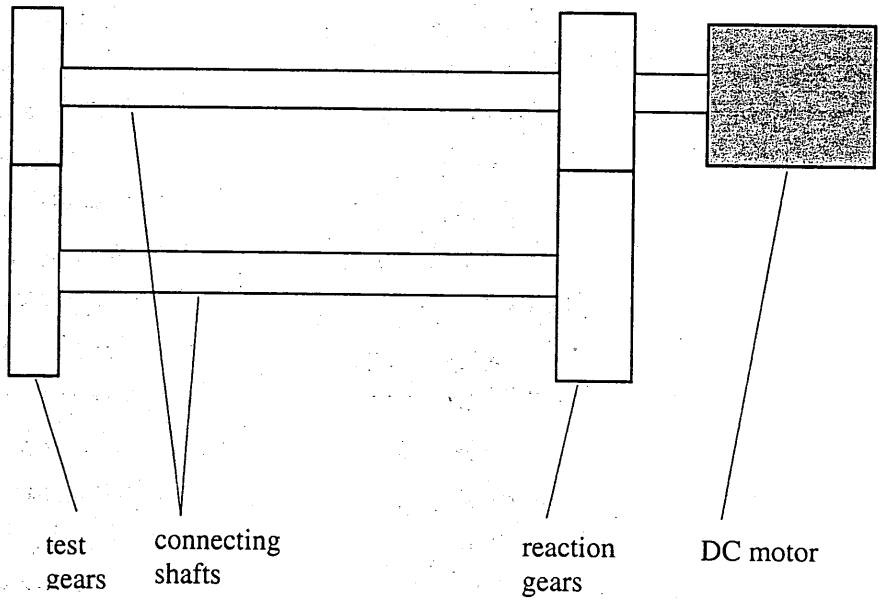

Figure 1. A four-square type gear test machine layout.

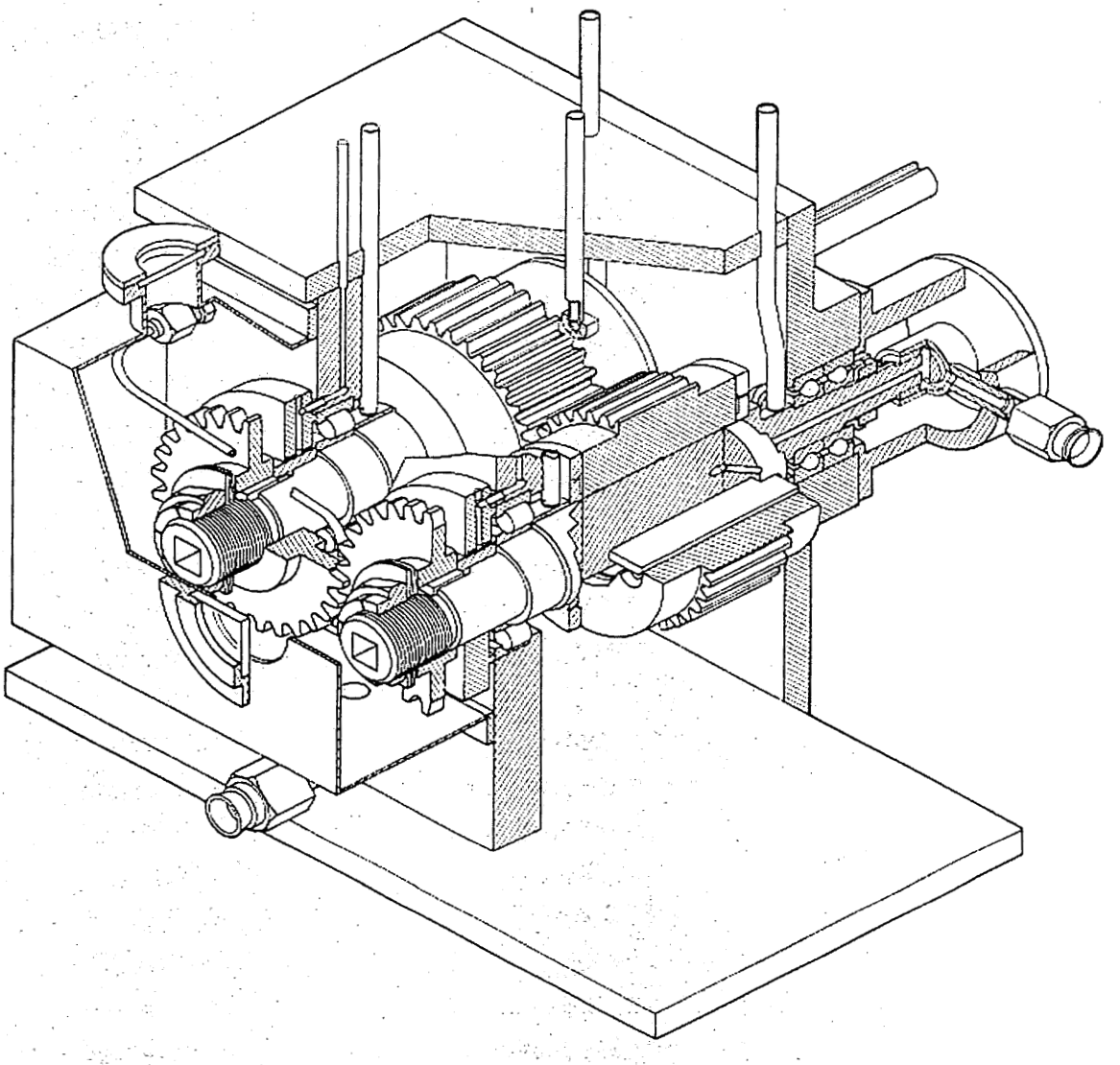

Figure 2. NASA gear durability test machine.

This study was formed by three major tasks: (1) assessment of the gear sets of the current test machine, (2) development of dynamic models, and (3) parametric studies and design recommendations. The following sections describe each task and the studies performed to achieve them.

2. Assessment of the Gear Sets of the Current GRC Test Machine

The current GRC test machine shown in Figure 2 includes a pair of unity ratio test spur gears meshed in an offset configuration such that the active face width is narrower than the gear face width. The reaction gear set is of the same unity ratio and the center distance as the test gear pair except different tooth counts. As a prerequisite to any detailed dynamic analysis of the current test rigs, the vibration excitation from both gear pairs must be quantified. Accordingly, this task involves (i) inspection of a number of test and reaction gears to determine whether their nominal dimensions characterize them accurately, and (ii) finite-element-based contact mechanics analyses of both test and reaction gear pairs to determine the parameters required by the dynamic models.

2.1. Test and Reaction Gear Tooth Surface Measurements

This task was performed by using a state-of-the-art gear coordinate measurement machine (CMM) available at the Center for Research (CGR) of the University of Toledo. One pair of brand-new test gears, a set of brand-new reaction gears and another set of used reaction gears were inspected. Figures 3 and 4 show these gears while being inspected on the gear CMM. Every tooth on each gear was inspected in both profile and lead directions. The tooth indexing errors were recorded as well.

Figures 5 to 7 illustrate CMM inspections of a typical unused test gear. In Figure 5, the profile traces of four representative teeth are shown. Overall quality of in profile direction is good. The intended profile tip relief differs slightly between the right and left flanks (for the right flank, 15-17 μm tip relief starting at 22 deg., and for the left flank, about 10 μm starting at 25 deg. roll angle). The lead charts of Figure 6 show no signs of lead errors and lead crown. Finally, the indexing

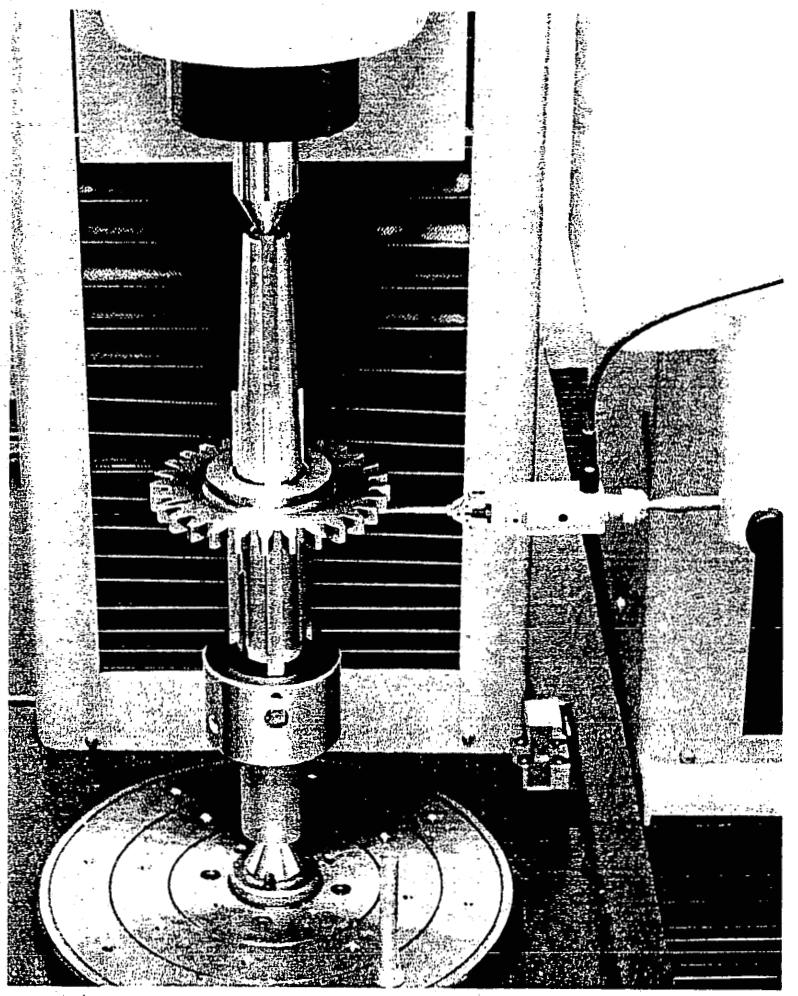

Figure 3. A test gear while being inspected on the gear CMM.

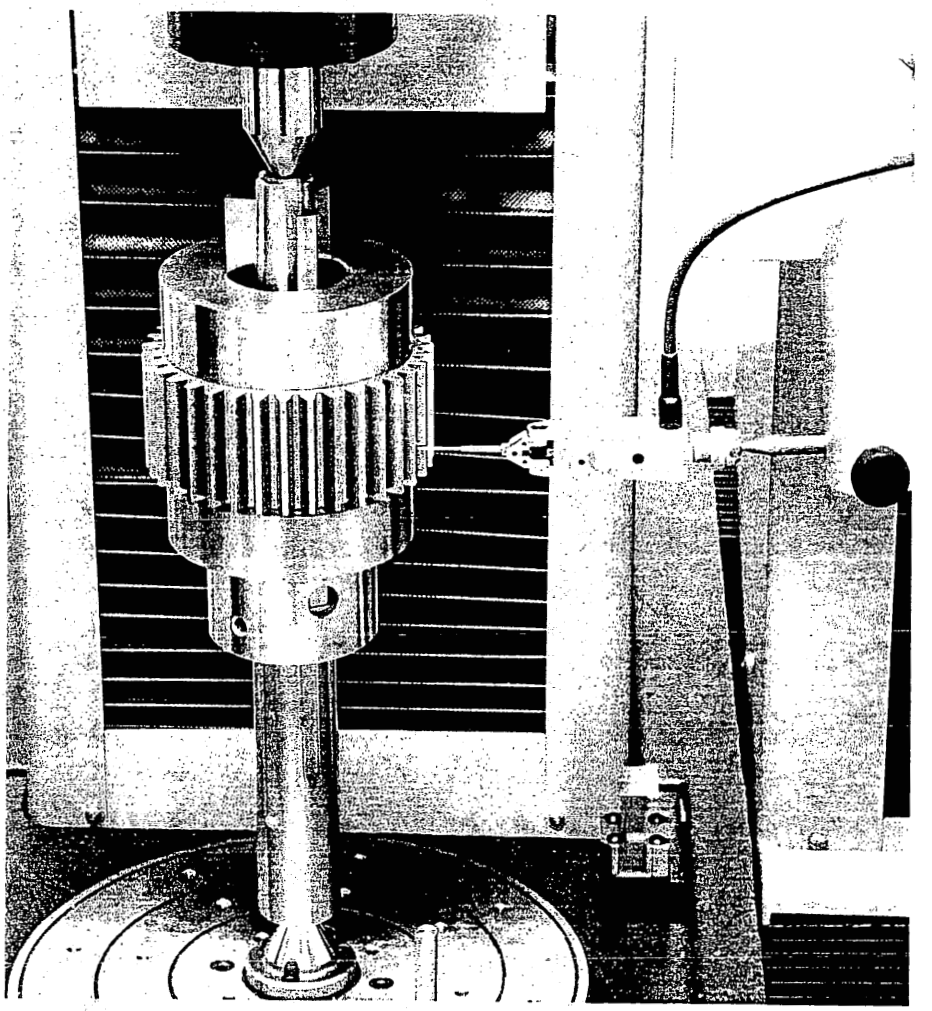

Figure 4. A reaction gear while being inspected on the gear CMM.

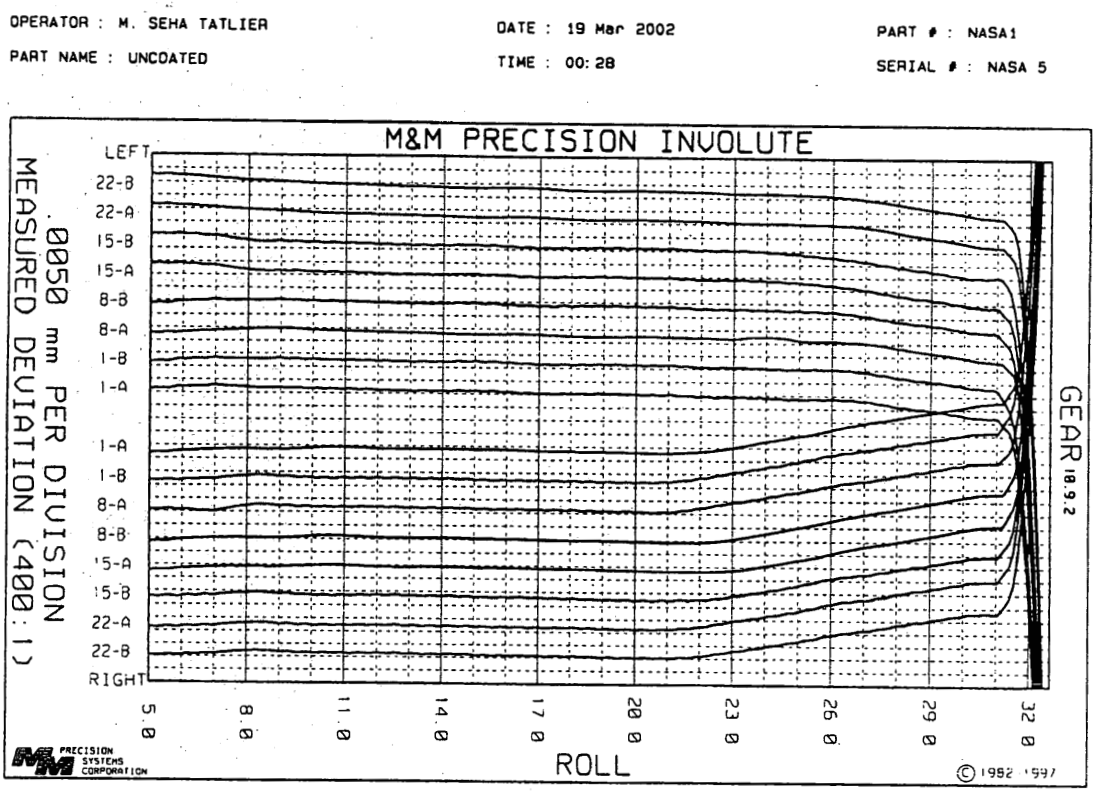

Figure 5. Profile inspections of a both flanks of four teeth on a typical test gear.

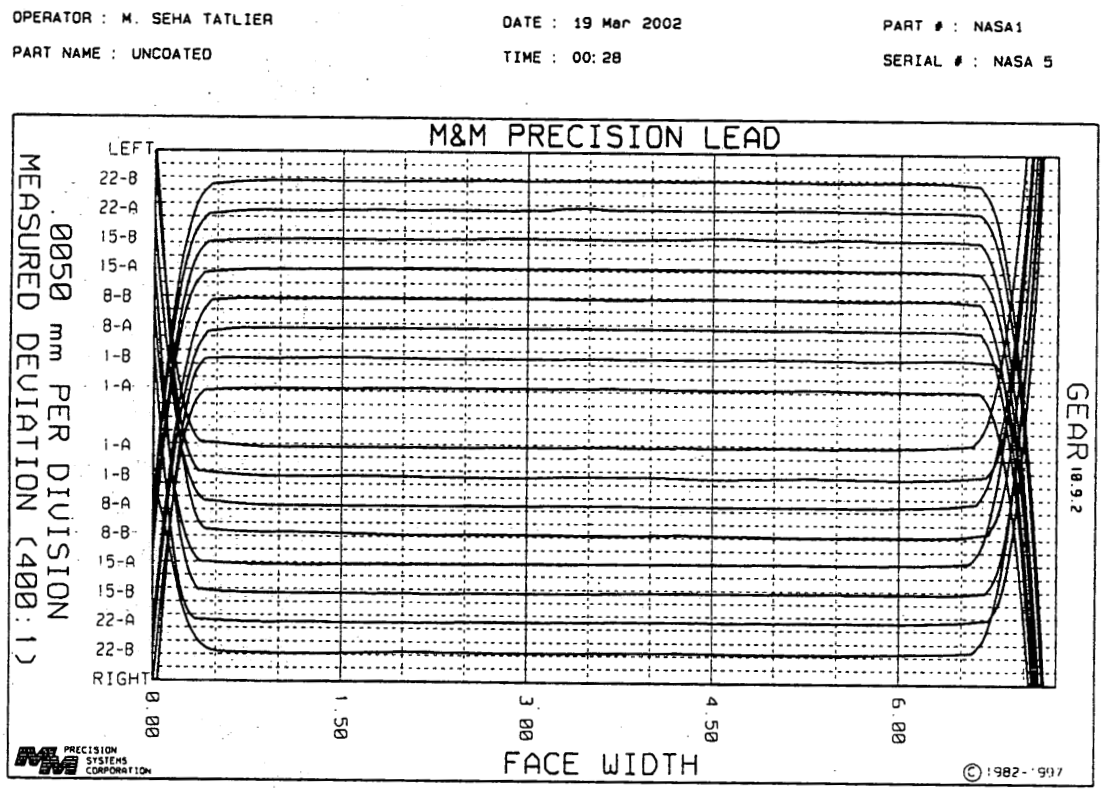

Figure 6. Lead inspections of a both flanks of four teeth on a typical test gear.

OPERATOR : M. SEHA TATLIER DATE : 19 Mar 2002 PART # : NASA1

PART NAME : UNCOATED TIME : 00:28 SERIAL # : NASA 5

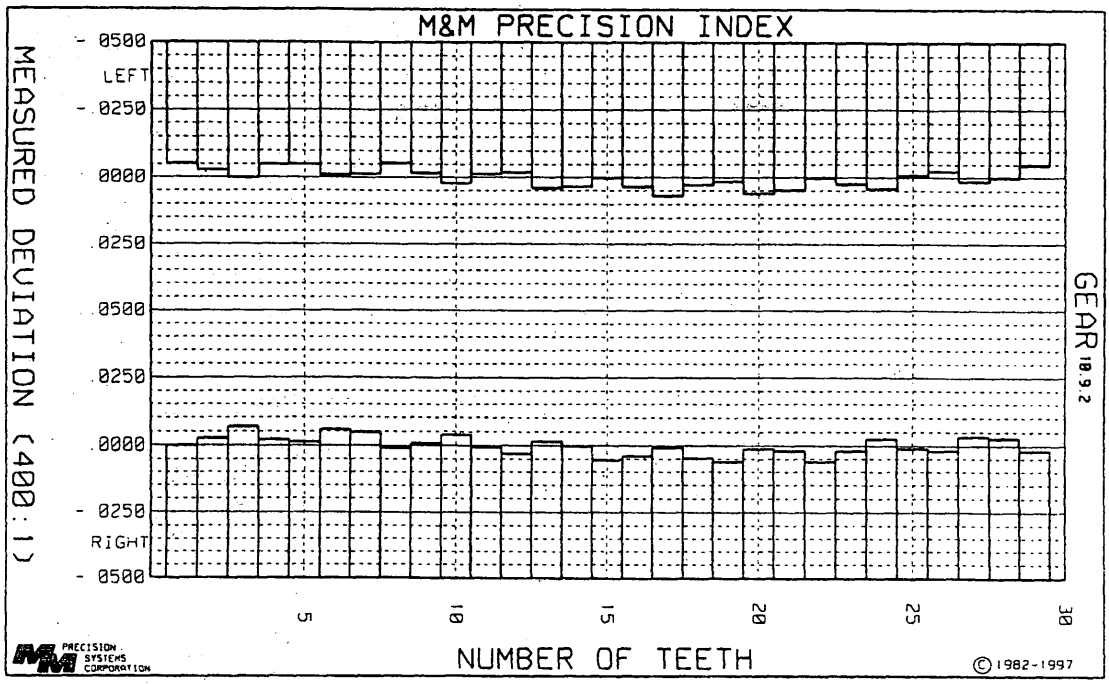

LEFT FLANK		
TOTAL INDEX VARIATION	.0125 mm	
WORST PITCH VARIATION	.0059 mm	TEETH 12 AND 13
WORST SPACING VARIATION	.0083 mm	TEETH 2, 3 AND 4
RIGHT FLANK		
TOTAL INDEX VARIATION	.0129 mm	
WORST PITCH VARIATION	-.0056 mm	TEETH 7 AND 8
WORST SPACING VARIATION	.0089 mm	TEETH 2, 3 AND 4
ANALYZED RUNOUT	.0068 mm	AT 238.4°

Figure 7. Measured indexing errors of a typical test gear.

errors shown in Figure 7 are within 12 μm suggesting that once-per-revolution errors are tightly controlled as well.

A number of new and used reaction gears were also inspected. Figures 8 to 10 show CMM inspections of a new reaction gear. In Figure 8, the profile traces of four representative teeth indicate that there is a slight tip relief (about 5 μm) starting at about 15 degrees roll angle. Overall quality of in profile direction is exceptional. The lead charts of Figure 9 also indicate very good quality. Finally, the indexing errors in Figure 10 show a slight sinusoidal variation (about 15 μm for this particular gear). For the other new and used reaction gears inspected, peak-to-peak indexing errors varied between 5 and 30 μm.

In summary, both test and reaction gears measured are high precision gears with very little profile and lead errors. The test gear teeth have no lead crown in agreement with the nominal design and have a linear tip relief close to the intended design value of 15 μm starting at a roll angle of 24.5 degrees. The reaction gears have slight profile modifications and no lead corrections. The amounts of one-per-revolution indexing errors are within the range of 5 to 30 μm in diameter. From these inspections, it was concluded that a contact mechanics analysis of the nominal gears would represent the real life conditions accurately, except the influence of the indexing errors of the reaction gear pairs.

2.2 Contact Mechanics Analyses

A finite element based contact mechanics analysis of both test gears (with and without face off-set) were carried out to determine (i) the average gear mesh stiffness values and (ii) loaded transmission error excitation harmonic amplitudes. Figures 11 and 12 illustrate a contact model of a test gear pair with and without face offset, respectively. A face offset of 3.3 mm has been used in durability tests to allow four tests to be performed per gear pair. A commercially available gear contact analysis model CAPP was used contact mechanics analyses. Figure 13 shows the contact mechanics model of the reaction gear set. The design parameters for both test and reaction gear sets are listed in Table 1. The analyses were carried out under quasi-static conditions at 16 discrete rotational positions per mesh cycle. A torque value of $T = 68.5$ N-m (50.5 ft-lb) was used in the analysis.

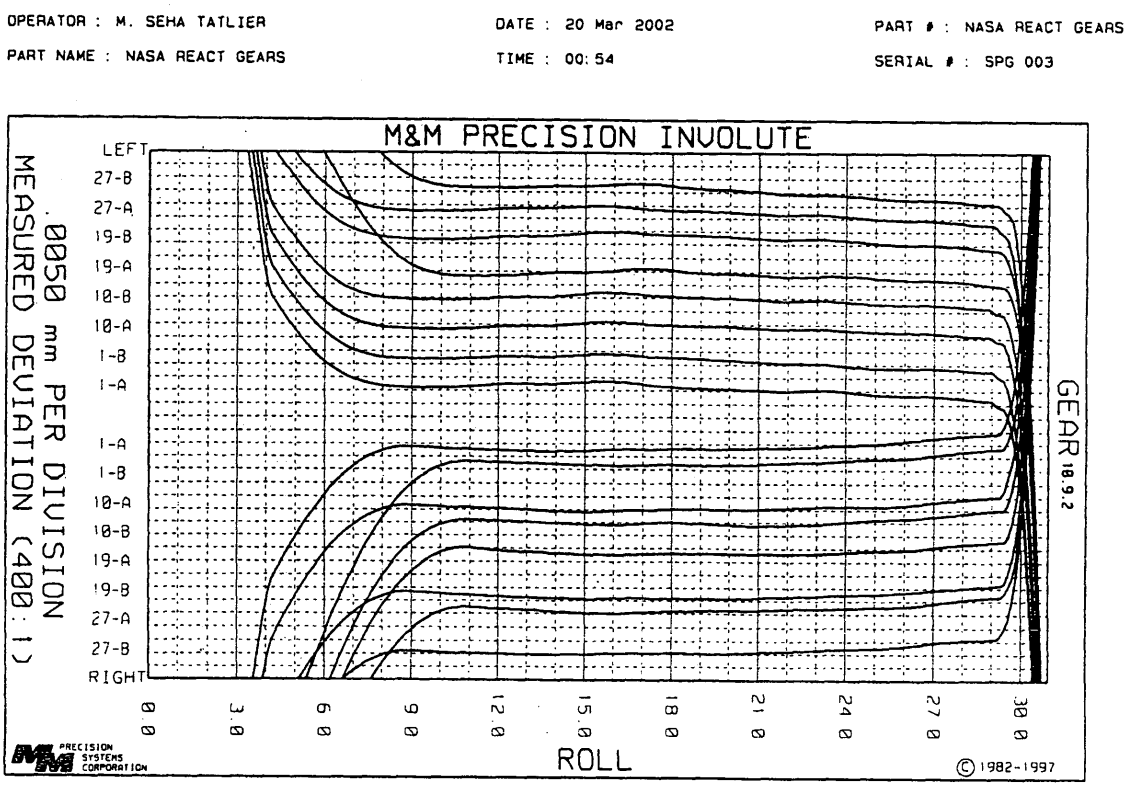

Figure 8. Profile inspections of both flanks of four teeth on a new reaction gear.

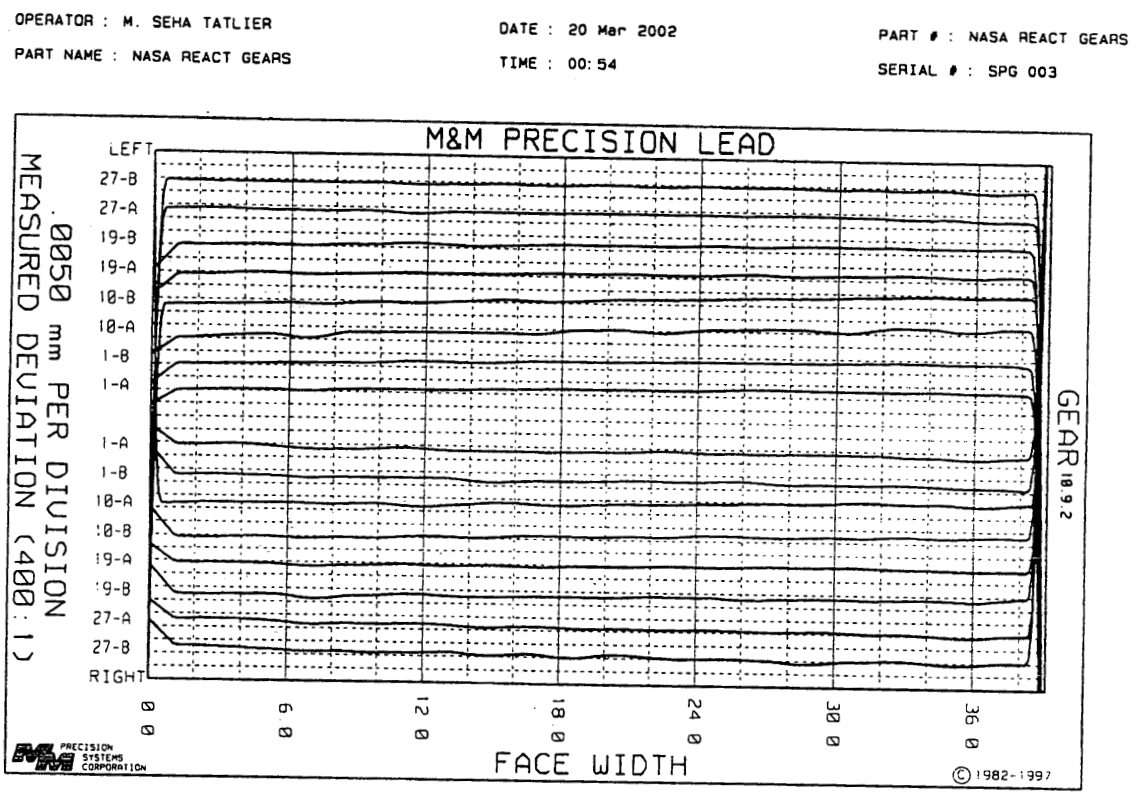

Figure 9. Lead inspections of both flanks of four teeth on a new reaction gear.

OPERATOR : M. SEHA TATLIER
DATE : 20 Mar 2002
PART # : NASA REACT GEARS
PART NAME : NASA REACT GEARS
TIME : 00:49
SERIAL # : SPG 003

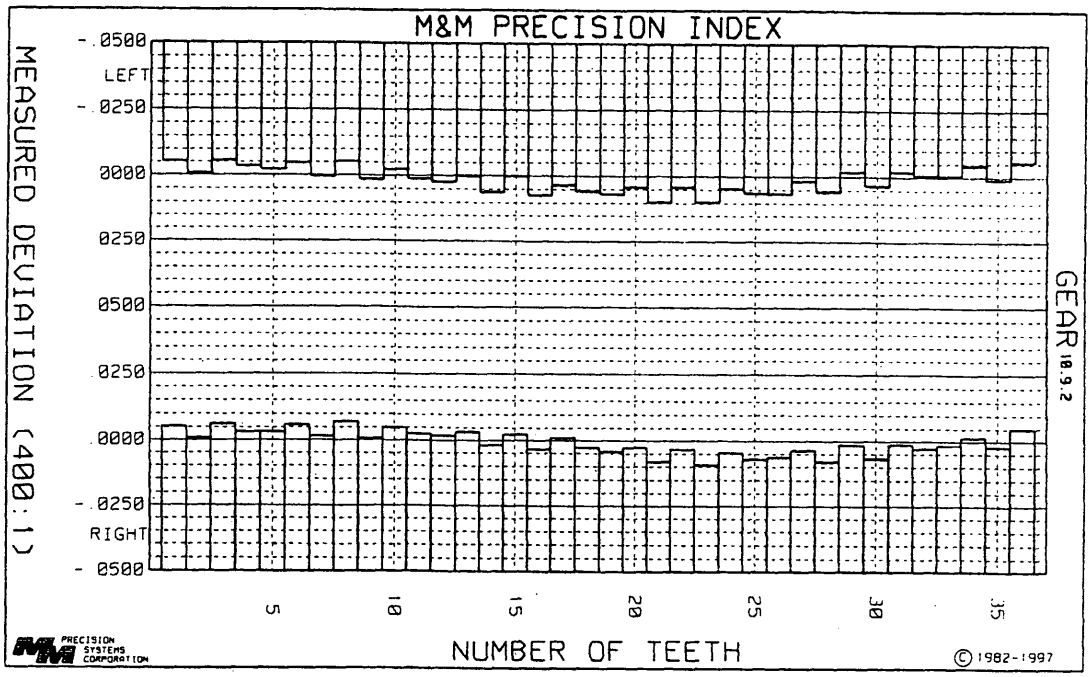

LEFT FLANK
TOTAL INDEX VARIATION .0152 mm
WORST PITCH VARIATION -.0075 mm TEETH 28 AND 29
WORST SPACING VARIATION .0129 mm TEETH 14, 15 AND 16

RIGHT FLANK
TOTAL INDEX VARIATION .0164 mm
WORST PITCH VARIATION .0070 mm TEETH 35 AND 1
WORST SPACING VARIATION .0119 mm TEETH 28, 29 AND 30

ANALYZED RUNOUT .0098 mm AT 233.8°

Figure 10. Measured indexing errors of a new reaction gear.

First, in order to establish the average mesh stiffness values, gear pairs were considered to have no modifications. In this case, any transmission error predicted must be due to the tooth deformations. The ratio of static gear mesh force applied to average value of the static transmission error is equal to the average gear mesh stiffness value:

$$\bar{k}_t = \frac{T}{r_{pt}\bar{\varepsilon}_t} \quad \text{and} \quad \bar{k}_r = \frac{T}{r_{pr}\bar{\varepsilon}_r}$$

where $\bar{k}$ is the average gear mesh stiffness value, r_p is the gear pitch radius, and $\bar{\varepsilon}$ is the average static transmission error. Subscripts t and r denote the test and reaction gears, respectively. Figures 14 and 15 show the static transmission error of unmodified test and reaction gear pairs as a function of gear rotation at $T = 68.5$ N-m. From these results, the average mesh stiffness values were determined to be

$$\bar{k}_t = \begin{cases} 8.57\times10^7 \ N/m & \textit{for offset gear pair} \\ 1.17\times10^8 \ N/m & \textit{for no offset} \end{cases} \quad \text{and} \quad \bar{k}_r = 6.18\times10^8 \ N/m.$$

The slight increase in the value of $\bar{k}_t$ for the case of no face offset is primarily due to an increase in the contact area. It is also noted that the reaction gear mesh is nearly 7 times stiffer than the test gear pair with face offset.

Next, the same test gear contact analyses were performed now for the gear pairs with the designed profile modifications (a 15.24 μm linear tip relief starting at a roll angle of 24.5 degrees). Figure 16 shows the loaded transmission error of the modified test gear pair both with and without the face offset. The Fast Fourier Transform (FFT) of the loaded transmission errors of Figure 16 yields the harmonic amplitudes of the gear mesh transmission error excitations, first three of which are listed in Table 2. Similarly, the transmission error of the reaction gear pair shown in Figure 15 was used to calculate the harmonic amplitudes of the reaction gear transmission error excitation that are also listed in Table 2.

Table 1

Design parameters of test and reaction gears of the NASA gear durability test machine.
(All dimensions are in mm unless specified)

	Test	Reaction
Number of teeth	28	35
Module	3.175	2.54
Circular pitch	9.975	7.98
Whole depth	7.62	6.35
Addendum	3.18	2.54
Chordal tooth thickness ref.	4.85	3.88
Pressure angle (deg)	20	20
Pitch diameter	88.9	88.9
Outside diameter	95.25	93.98
Root fillet radius	1.02 to 1.52	--
Measurement over pins	96.03 to 96.30	--
Pin diameter	5.49	--
Backlash ref.	0.254	0.254
Linear tip relief	0.01524	--
Roll angle of tip relief (deg)	24.5	--

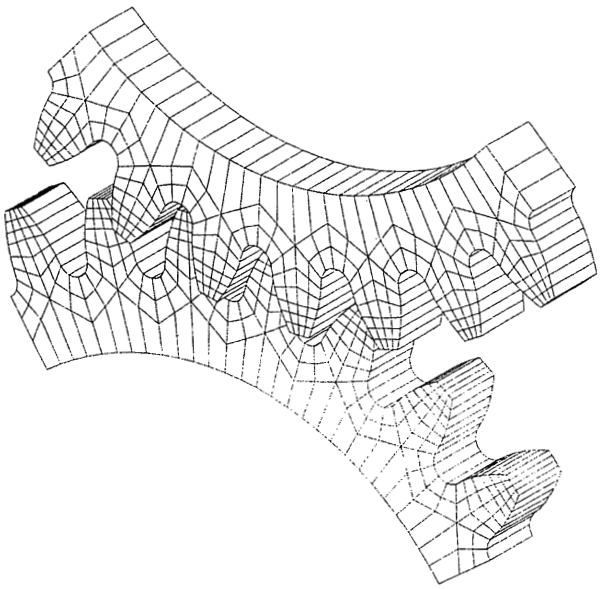

Figure 11. Contact mechanics model of a test gear pair with face offset.

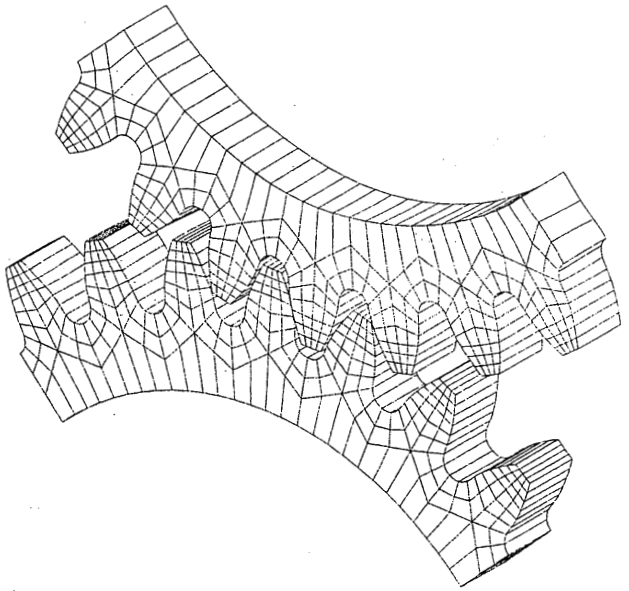

Figure 12. Contact mechanics model of a test gear pair without face offset.

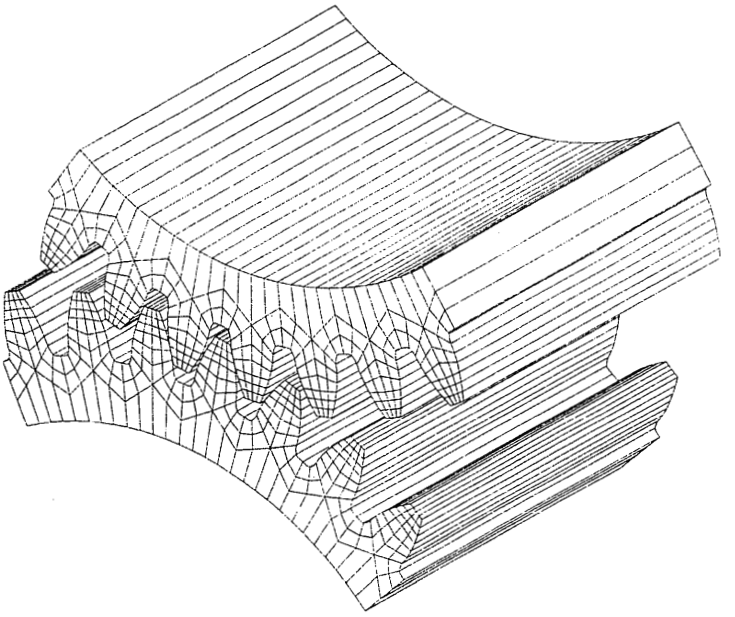

Figure 13. Contact mechanics model of a reaction gear pair.

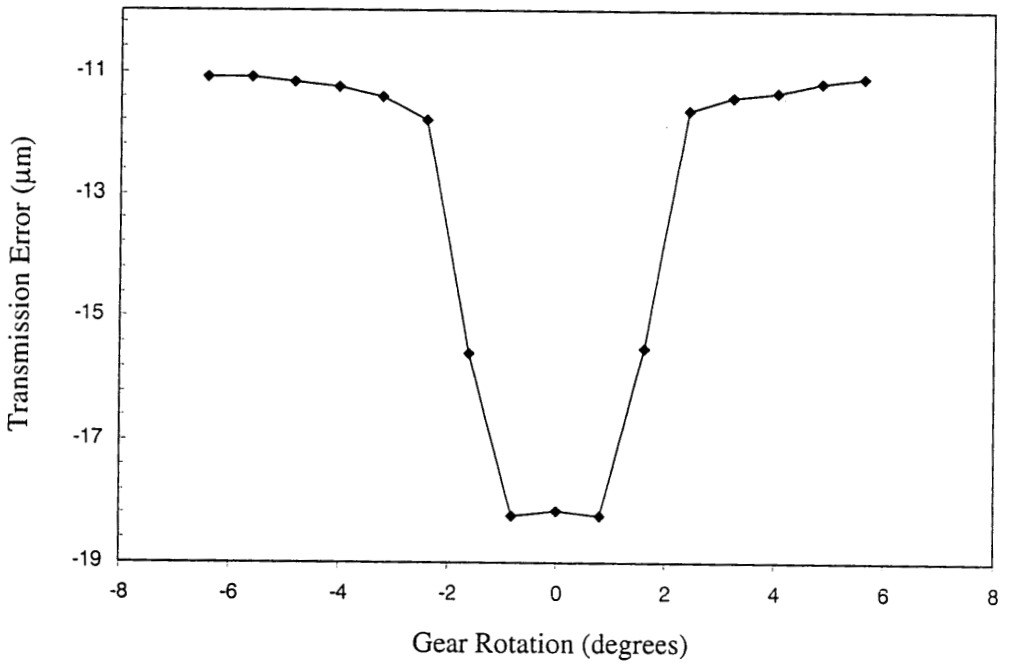

Figure 14. Static transmission error of an unmodified test gear pair without offset

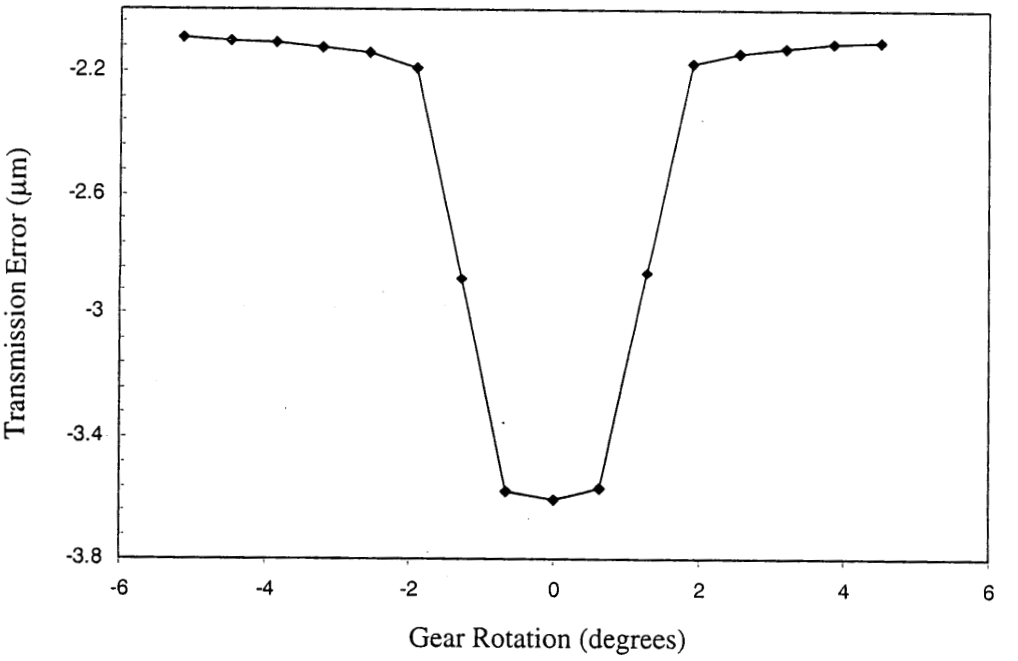

Figure 15. Static transmission error of the reaction gear pair.

Table 2

Transmission error harmonic amplitudes of test and reaction gears of the NASA gear durability test machine (in μm).

Harmonic Index, i	Reaction pair	Test pair with with face offset	Test gear pair without face offset
1	0.67	2.26	0.56
2	0.42	1.11	0.30
3	0.17	0.04	0.13

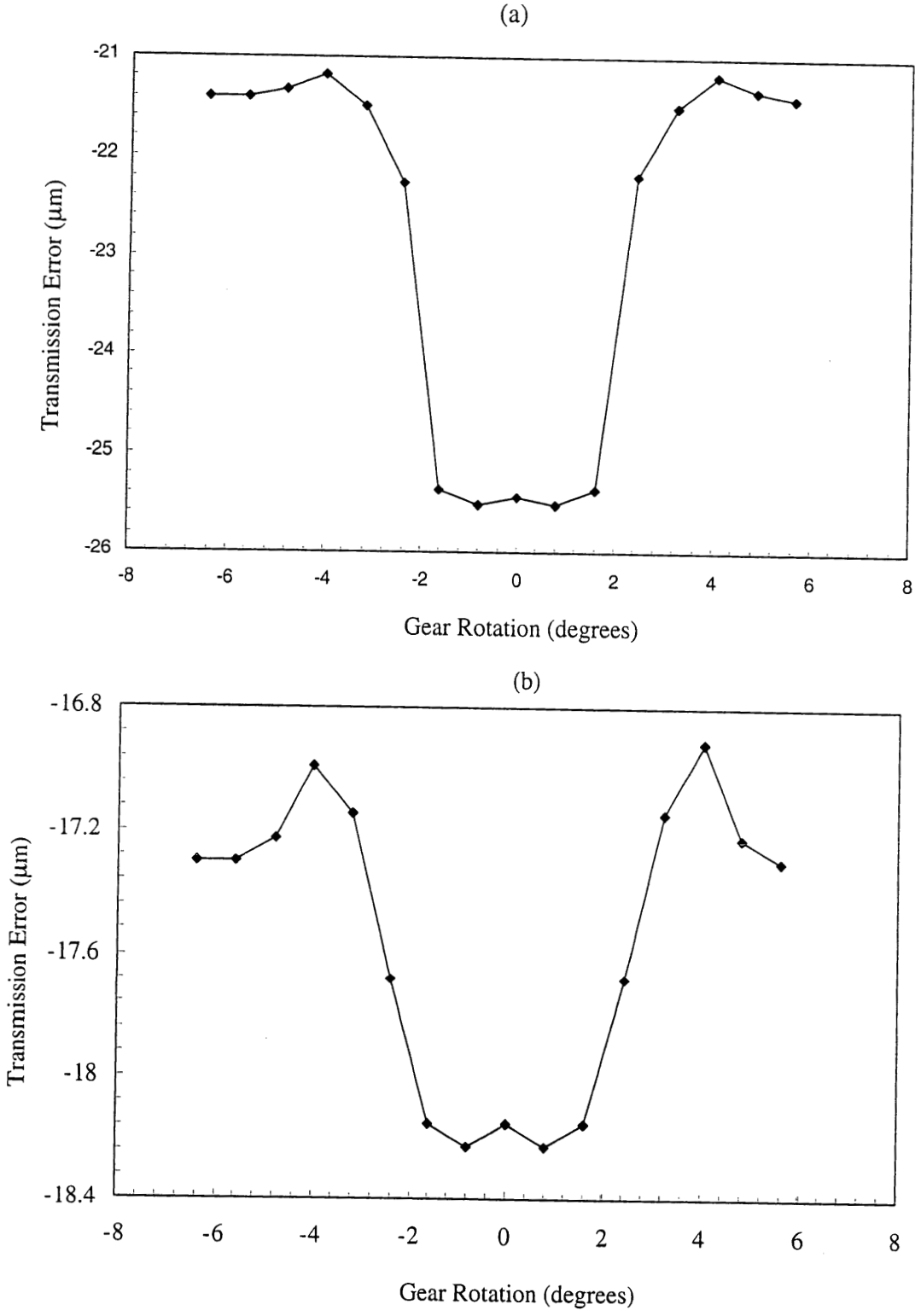

Figure 16. Loaded transmission error of a modified test gear pair (a) with offset, and (b) without offset.

3. Dynamic Models

As stated earlier, two major objectives of the project are to (i) investigate whether any transverse or torsional resonance(s) exists near the operating speed of interest at the given torque value, and (ii) determine the stiffness properties of the for the connecting shaft structures and inertias between the test and reaction gear sets are suitable for isolation of the reaction gearbox from the test gearbox. Two dynamic models will be developed to achieve these objectives. The models will also be employed to define solutions if there are potential resonance and/or vibration isolation problems associated with the current test rig.

3.1. Torsional Dynamic Model

A purely torsional linear dynamic model of a NASA four-square gear durability test machine shown in Figure 2 is developed here as shown in Figure 17. Here, each gear of base radius r and polar mass moment of inertia J is assumed to be rigid except the teeth in contact. Gears are also assumed to vibrate in torsional direction only defined by rotational alternating displacement θ. The gear mesh interface of the test gears is represented by a linear gear mesh stiffness $\bar{k}_t$ and a periodic static transmission error excitation $e_t(t)$. Similarly, $\bar{k}_r$ and $e_r(t)$ represent the mean mesh stiffness and the transmission error excitation of the reaction gear pair.

3.1.1. Equations of Motion

Considering that the subscripts $t1$ and t2 represent test gears on shafts 1 and 2 and subscripts $r1$ and $r2$ represent the reaction gears on shafts 1 and 2, the equations of motion of the four-degree-of-freedom dynamic model are given as

$$
\left.
\begin{aligned}
&J_{t1}\ddot{\theta}_{t1} + r_{t1}c_t\left[r_{t1}\dot{\theta}_{t1} + r_{t2}\dot{\theta}_{t2}\right] + r_{t1}\bar{k}_t\left[r_{t1}\theta_{t1} + r_{t2}\theta_{t2} - e_t(t)\right] + k_{s1}(\theta_{t1} - \theta_{r1}) = 0 \\
&J_{t2}\ddot{\theta}_{t2} + r_{t2}c_t\left[r_{t1}\dot{\theta}_{t1} + r_{t2}\dot{\theta}_{t2}\right] + r_{t2}\bar{k}_t\left[r_{t1}\theta_{t1} + r_{t2}\theta_{t2} - e_t(t)\right] + k_{s2}(\theta_{t2} - \theta_{r2}) = 0 \\
&J_{r2}\ddot{\theta}_{r2} + r_{r2}c_r\left[r_{r1}\dot{\theta}_{r1} + r_{r2}\dot{\theta}_{r2}\right] + r_{r2}\bar{k}_r\left[r_{r1}\theta_{r1} + r_{r2}\theta_{r2} - e_r(t)\right] - k_{s2}(\theta_{t2} - \theta_{r2}) = 0 \\
&J_{r1}\ddot{\theta}_{r1} + r_{r1}c_r\left[r_{r1}\dot{\theta}_{r1} + r_{r2}\dot{\theta}_{r2}\right] + r_{r1}\bar{k}_r\left[r_{r1}\theta_{r1} + r_{r2}\theta_{r2} - e_r(t)\right] - k_{s1}(\theta_{t1} - \theta_{r1}) = 0
\end{aligned}
\right\} \quad (1)
$$

where c_t and c_r represent the gear mesh damping values that are not shown in Figure 17 for clarity purposes, and k_{s1} and k_{s2} are the torsional stiffness values of the shafts connecting the test gears to the reaction gears. The polar mass moments of inertia of these shafts are divided into two and lumped to the inertias of the gears at both sides. In order to obtain a matrix form of the equations of motion, equation (1) can be put into the form:

$$
\left.
\begin{aligned}
&J_{t1}\ddot{\theta}_{t1} + r_{t1}^2 c_t\dot{\theta}_{t1} + r_{t1}r_{t2}c_t\dot{\theta}_{t2} + (r_{t1}^2\bar{k}_t + k_{s1})\theta_{t1} + r_{t1}r_{t2}\bar{k}_t\theta_{t2} - k_{s1}\theta_{r1} = r_{t1}\bar{k}_t e_t(t) \\
&J_{t2}\ddot{\theta}_{t2} + r_{t1}r_{t2}c_t\dot{\theta}_{t1} + r_{t2}^2 c_t\dot{\theta}_{t2} + r_{t1}r_{t2}\bar{k}_t\theta_{t1} + (r_{t2}^2\bar{k}_t + k_{s2})\theta_{t2} - k_{s2}\theta_{r2} = r_{t2}\bar{k}_t e_t(t) \\
&J_{r2}\ddot{\theta}_{r2} - k_{s2}\theta_{t2} + r_{r2}^2 c_r\dot{\theta}_{r2} + r_{r1}r_{r2}c_t\dot{\theta}_{r1} + r_{r1}r_{r2}\bar{k}_r\theta_{r1} + (r_{r2}^2\bar{k}_t + k_{s2})\theta_{r2} = r_{r2}\bar{k}_r e_r(t) \\
&J_{r1}\ddot{\theta}_{r1} - k_{s1}\theta_{t1} + r_{r1}r_{r2}c_r\dot{\theta}_{r2} + r_{r1}^2 c_r\dot{\theta}_{r1} + r_{r1}r_{r2}\bar{k}_r\theta_{r2} + (r_{r1}^2\bar{k}_r + k_{s1})\theta_{r1} = r_{r1}\bar{k}_r e_r(t)
\end{aligned}
\right\} \quad (2)
$$

The equations of motion are then written in matrix form as

$$
\mathbf{M}\ddot{\mathbf{q}}(t) + \mathbf{C}\dot{\mathbf{q}}(t) + \mathbf{K}\mathbf{q}(t) = \mathbf{F}(t) \quad (3a)
$$

where the mass, damping and stiffness matrices are define from equations (2) as

$$
\mathbf{M} = \begin{bmatrix} J_{t1} & 0 & 0 & 0 \\ 0 & J_{t2} & 0 & 0 \\ 0 & 0 & J_{r2} & 0 \\ 0 & 0 & 0 & J_{r1} \end{bmatrix}, \quad (3b)
$$

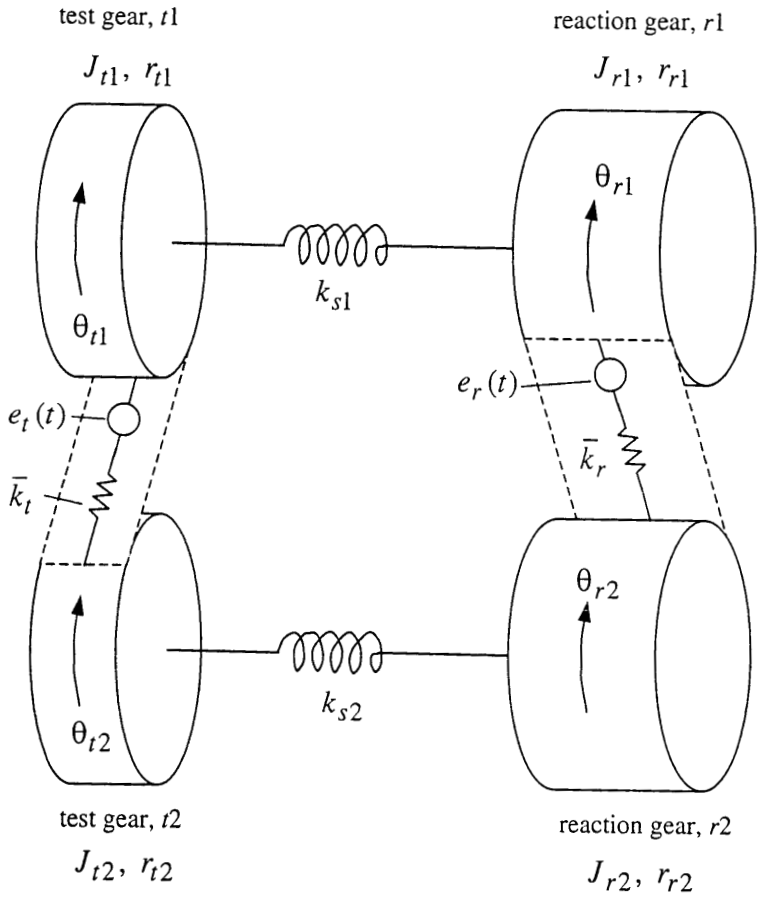

Figure 17. A four-degree-of-freedom torsional model of a four-square test machine.

$$\mathbf{C} = \begin{bmatrix} r_{t1}^2 c_t & r_{t1} r_{t2} c_t & 0 & 0 \\ r_{t1} r_{t2} c_t & r_{t2}^2 c_t & 0 & 0 \\ 0 & 0 & r_{r2}^2 c_r & r_{r1} r_{r2} c_r \\ 0 & 0 & r_{r1} r_{r2} c_r & r_{r1}^2 c_t \end{bmatrix} \tag{3c}$$

$$\mathbf{K} = \begin{bmatrix} r_{t1}^2 \bar{k}_t + k_{s1} & r_{t1} r_{t2} \bar{k}_t & 0 & -k_{s1} \\ r_{t1} r_{t2} \bar{k}_t & r_{t2}^2 \bar{k}_t + k_{s2} & -k_{s2} & 0 \\ 0 & -k_{s2} & r_{r2}^2 \bar{k}_r + k_{s2} & r_{r1} r_{r2} \bar{k}_r \\ -k_{s1} & 0 & r_{r1} r_{r2} \bar{k}_r & r_{r1}^2 \bar{k}_t + k_{s1} \end{bmatrix} \tag{3d}$$

The displacement vector and the external forcing vector are defined as

$$\mathbf{q}(t) = \begin{Bmatrix} \theta_{t1}(t) \\ \theta_{t2}(t) \\ \theta_{r2}(t) \\ \theta_{r1}(t) \end{Bmatrix}, \qquad \mathbf{F}(t) = \begin{Bmatrix} r_{t1} \bar{k}_t e_t(t) \\ r_{t2} \bar{k}_t e_t(t) \\ r_{r2} \bar{k}_r e_r(t) \\ r_{r1} \bar{k}_r e_r(t) \end{Bmatrix}. \tag{3e,f}$$

The excitation function $e_t(t)$ at the mesh of the test gear pair includes only the once/mesh components of the static transmission error as index errors of actual gear specimens were measured earlier to be insignificant

$$e_t(t) = \sum_{i=1}^{L} \tilde{e}_{ti} \sin[i\omega_t t + \varphi_{ti}] \tag{4}$$

where $\tilde{e}_{ti}$ is the i-th harmonic amplitude of the test gear pair transmission error as listed in Table 2. Here, the test gear mesh frequency is defined as $\omega_t = 2\pi\Omega_{s1} Z_{t1} / 60$ where Ω_{s1} is the rotational speed of the first shaft in *rpm* and Z_{t1} is the number of teeth on the first test gear. As evident form equation (4), no once/revolution component of the test gear mesh excitation is included since the pitch line run-out errors, index errors and spacing errors of the actual test gears were very low as shown in Figure 7.

Meanwhile, the excitation function $e_r(t)$ at the mesh of the reaction gear pair includes not only the once/mesh components of the static transmission error but also once/revolution components of each reaction gear since indexing errors of these gears were measured to be not negligible as shown in Figure 10. Accordingly $e_r(t)$ is defined as

$$e_r(t) = \sum_{i=1}^{L} \tilde{e}_{ri} \sin[i\omega_r t + \varphi_{ri}] + E_{r1} \sin\left[\frac{\omega_r}{Z_{r1}} t + \gamma_{r1}\right] - E_{r2} \sin\left[\frac{\omega_r}{Z_{r2}} t + \gamma_{r2}\right]. \tag{5}$$

Here $\tilde{e}_{ri}$ is the i-th harmonic mesh order amplitude of the reaction gear pair as listed in Table 2, and the reaction gear mesh frequency is defined as $\omega_r = 2\pi\Omega_{s1} Z_{r1} / 60$ where Z_{r1} is the number of teeth on the first reaction gear. In addition, the once/revolution errors of both reaction gears are included in harmonic form having amplitudes E_{r1} and E_{r2} and initial assembly position angles γ_{r1} and γ_{r2}. The frequency of these two excitations are ω_r / Z_{r1} and ω_r / Z_{r2}.

3.1.2. Natural Modes and Forced Response

The solution of the Eigen Value problem governing equation (3a) yields the natural frequencies ω_i and the corresponding mode shapes Φ_i ($i = 1$ to 4). As the system shown in Figure 17 is a linear one, the forced response to the excitations of equations (4) and (5) can be calculated by using the Modal Summation Technique [1]. In order to apply this technique, first the forcing vector $\mathbf{F}(t)$ of equation (3f) is put in the form

$$\begin{aligned}\mathbf{F}(t) = &\begin{Bmatrix} r_{t1} \\ r_{t2} \\ 0 \\ 0 \end{Bmatrix} \bar{k}_t \sum_{i=1}^{L} \tilde{e}_{ti} \sin[i\omega_t t + \varphi_{ti}] + \begin{Bmatrix} 0 \\ 0 \\ r_{r2} \\ r_{r1} \end{Bmatrix} \bar{k}_r \sum_{i=1}^{L} \tilde{e}_{ri} \sin[i\omega_r t + \varphi_{ri}] \\ &+ \begin{Bmatrix} 0 \\ 0 \\ r_{r2} \\ r_{r1} \end{Bmatrix} \bar{k}_r E_{r1} \sin\left[\frac{\omega_r}{Z_{r1}} t + \gamma_{r1}\right] - \begin{Bmatrix} 0 \\ 0 \\ r_{r2} \\ r_{r1} \end{Bmatrix} \bar{k}_r E_{r2} \sin\left[\frac{\omega_r}{Z_{r2}} t + \gamma_{r2}\right]\end{aligned} \tag{6}$$

The forced response $\mathbf{q}(t)$ is then defined as

$$\mathbf{q}(t) = \begin{Bmatrix} r_{t1} \\ r_{t2} \\ 0 \\ 0 \end{Bmatrix} \bar{k}_t \sum_{i=1}^{L} \Lambda_{ti} \tilde{e}_{ti} \sin\left[i\omega_t t + \varphi_{ti} + \Gamma_{ti}\right] + \begin{Bmatrix} 0 \\ 0 \\ r_{r2} \\ r_{r1} \end{Bmatrix} \bar{k}_r \sum_{i=1}^{L} \Lambda_{ri} \tilde{e}_{ri} \sin\left[i\omega_r t + \varphi_{ri} + \Gamma_{ri}\right]$$
$$+ \begin{Bmatrix} 0 \\ 0 \\ r_{r2} \\ r_{r1} \end{Bmatrix} \bar{k}_r \Lambda_{E1} E_{r1} \sin\left[\frac{\omega_r}{Z_{r1}} t + \gamma_{r1} + \Gamma_{E1}\right] - \begin{Bmatrix} 0 \\ 0 \\ r_{r2} \\ r_{r1} \end{Bmatrix} \bar{k}_r \Lambda_{E2} E_{r2} \sin\left[\frac{\omega_r}{Z_{r2}} t + \gamma_{r2} + \Gamma_{E2}\right] \tag{7a}$$

where the dynamic compliance matrices are

$$\Lambda_{ti} = \sum_{s=1}^{S} \frac{\Phi_s \Phi_s{}^T}{(\omega_s{}^2 - i^2 \omega_t{}^2 + 2jr\zeta_s \omega_s \omega_t)}, \tag{7b}$$

$$\Lambda_{ri} = \sum_{s=1}^{S} \frac{\Phi_s \Phi_s{}^T}{(\omega_s{}^2 - i^2 \omega_r{}^2 + 2jr\zeta_s \omega_s \omega_r)}, \tag{7c}$$

$$\Lambda_{E1} = \sum_{s=1}^{S} \frac{\Phi_s \Phi_s{}^T}{(\omega_s{}^2 - \left(\frac{\omega_r}{Z_{r1}}\right)^2 + \frac{2jr\zeta_s \omega_s \omega_r}{Z_{r1}})}, \tag{7d}$$

$$\Lambda_{E2} = \sum_{s=1}^{S} \frac{\Phi_s \Phi_s{}^T}{(\omega_s{}^2 - \left(\frac{\omega_r}{Z_{r2}}\right)^2 + \frac{2jr\zeta_s \omega_s \omega_r}{Z_{r2}})}. \tag{7e}$$

In above equations, L is the number of static transmission error harmonics that must be included in the analysis. Typically, it is sufficient to set $L = 3$ for spur gears as the higher harmonic amplitudes ($i > 3$) are negligibly small. S is the total number of degrees of freedom considered in the model. For the system of Figure 17, $S = 4$.

3.2. Three-dimensional Dynamic Model

As the torsional model proposed in the previous section should be sufficient for predicting the torsional natural modes and for investigating the vibration transmission/isolation issues, it is not capable of predicting transverse vibrations such as bearing vibrations and shaft bending vibrations. Such motions should become important especially when the shafts connecting the test and reaction gear sets are made more flexible. In this section, a transverse-torsional model of the system shown in Figure 1 will be developed. The model will be based on a general formulation to analyze any two shafts connected to each other through two separate gear meshes. This general model is to have the following capabilities:

- The model should include transverse, torsional, axial and rotational (bending) motions of the gear pairs that can be of spur or helical type.
- The model should be capable of simulating any shaft geometries including variable cross-sections, and the hollow shafts. The shaft transverse, torsional, axial and bending motions should all be included in the model.
- Any couplings, flywheels and rigid inertias that are mounted on the shafts including the rotatory inertia of the DC motor can be included.
- The model should have the ability to included any number of rolling element bearings of any type supporting the shafts at specified locations positioned at any location on the shafts

This model will be obtained by expanding an already existing geared rotor dynamics model [2]. This model was developed to study the coupled spur gear-shaft-bearing dynamics of a two-shaft, single-gear pair system and later expanded to include three shaft gear reduction units [3]. A lumped-parameter model of gear pair was combined with a finite element model of the shafts to predict the natural modes and the forced response due to static transmission error excitation. This model will be modified to include axial and bending motions of the shafts and gears to include helical gears, and a second gear pair coupling will be added to obtain the model of any four-square type closed-loop arrangement. The model will be made general such that any system of the same layout can be analyzed to allow parametric design optimization studies. In the following sections, the model formulation will be outlined. Only the essential details will be given here as further details can be found in references [2, 3].

3.2.1 Overall Shaft Matrices

The general system shown in Figure 1 has two parallel-axis shafts connected to each other at two places through spur or helical gears. Finite element model of each shaft can be developed by using Euler-Bernoelli beam elements [4]. Considering a finite element ℓ on one of the shafts defined by two nodes ℓ and $\ell+1$ as shown in Figure 18, the stiffness and mass/inertia matrices of this ℓ-th shaft (rotor) element are given as a summation of bending, torsion and axial components as

$$\mathbf{k}_{s\ell} = (\mathbf{k}_{s\ell})_{bending} + (\mathbf{k}_{s\ell})_{torsion} + (\mathbf{k}_{s\ell})_{axial}, \tag{8}$$

$$\mathbf{m}_{s\ell} = (\mathbf{m}_{s\ell})_{bending+axial} + (\mathbf{m}_{s\ell})_{rotation} + (\mathbf{m}_{s\ell})_{torsion} \tag{9}$$

where the individual components of $\mathbf{k}_{s\ell}$ and $\mathbf{m}_{s\ell}$ are given in Reference [3]. These shaft element matrices of dimension 12 can be put into the form

$$\mathbf{k}_{s\ell} = \begin{bmatrix} (\mathbf{k}_{11})_\ell & (\mathbf{k}_{21})_\ell^T \\ (\mathbf{k}_{21})_\ell & (\mathbf{k}_{22})_\ell \end{bmatrix}, \qquad \mathbf{m}_{s\ell} = \begin{bmatrix} (\mathbf{m}_{11})_\ell & (\mathbf{m}_{21})_\ell^T \\ (\mathbf{m}_{21})_\ell & (\mathbf{m}_{22})_\ell \end{bmatrix}. \tag{10,11}$$

Starting with the first shaft, if the shaft is defined by m_1 finite rotor elements ($\ell = 1, 2, \ldots, m_1$), the stiffness and mass matrices of the entire shaft 1 can be assembled as:

$$\mathbf{K}_{s1} = \begin{bmatrix} (\mathbf{k}_{11})_1 & & & & \textit{symmetric} \\ (\mathbf{k}_{21})_1 & (\mathbf{k}_{22})_1 + (\mathbf{k}_{11})_2 & & & \\ \mathbf{0} & (\mathbf{k}_{21})_2 & (\mathbf{k}_{22})_2 + (\mathbf{k}_{11})_3 & & \\ \vdots & \vdots & \vdots & \ddots & \\ \mathbf{0} & \mathbf{0} & \mathbf{0} & \cdots & (\mathbf{k}_{22})_{(m_1-1)} + (\mathbf{k}_{11})_{m_1} \\ \mathbf{0} & \mathbf{0} & \mathbf{0} & \cdots & (\mathbf{k}_{21})_{m_1} \qquad (\mathbf{k}_{22})_{m_1} \end{bmatrix} \tag{12}$$

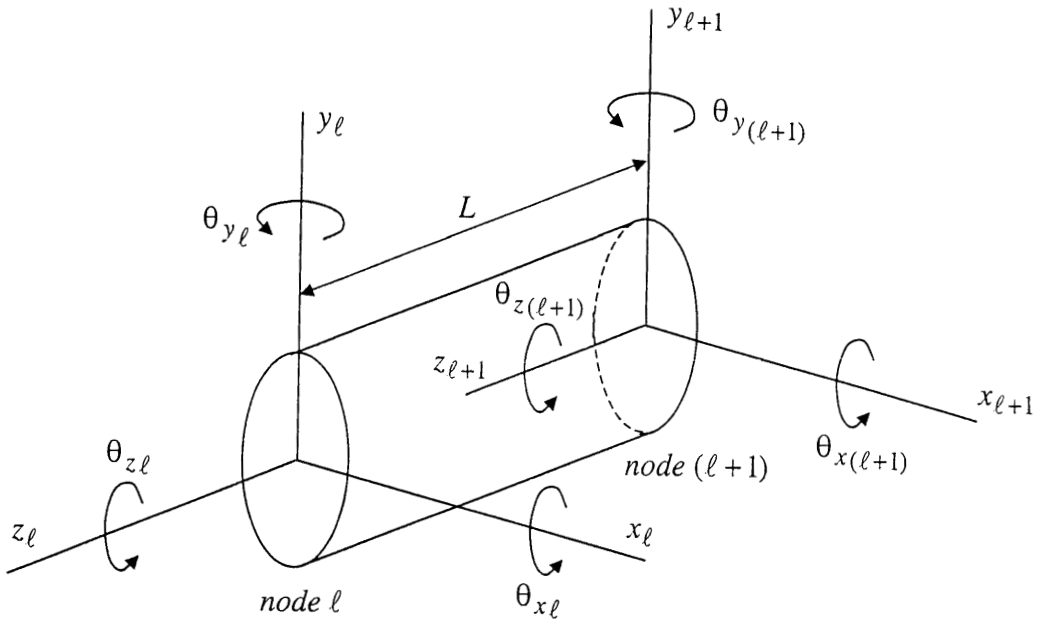

Figure 18. A finite shaft (rotor) element [3].

$$\mathbf{M}_{s1}=\begin{bmatrix} (\mathbf{m}_{11})_1 & & & & \textit{symmetric} & \\ (\mathbf{m}_{21})_1 & (\mathbf{m}_{22})_1+(\mathbf{m}_{11})_2 & & & & \\ \mathbf{0} & (\mathbf{m}_{21})_2 & (\mathbf{m}_{22})_2+(\mathbf{m}_{11})_3 & & & \\ \vdots & \vdots & \vdots & \ddots & & \\ \mathbf{0} & \mathbf{0} & \mathbf{0} & \cdots & (\mathbf{m}_{22})_{(m_1-1)}+(\mathbf{m}_{11})_{m_1} & \\ \mathbf{0} & \mathbf{0} & \mathbf{0} & \cdots & (\mathbf{m}_{21})_{m_1} & (\mathbf{m}_{22})_{m_1} \end{bmatrix} \tag{13}$$

The above formulation is applied to the second shaft that is described by a total of m_2 finite elements to obtain $\mathbf{K}_{s2}$ and $\mathbf{M}_{s2}$. The overall shaft stiffness $\mathbf{K}_s$ and mass $\mathbf{M}_s$ matrices are then assembled as

$$\mathbf{K}_s=\begin{bmatrix} \mathbf{K}_{s1} & \mathbf{0} \\ \mathbf{0} & \mathbf{K}_{s2} \end{bmatrix}, \qquad \mathbf{M}_s=\begin{bmatrix} \mathbf{M}_{s1} & \mathbf{0} \\ \mathbf{0} & \mathbf{M}_{s2} \end{bmatrix} \tag{14a,b}$$

Both $\mathbf{K}_s$ and $\mathbf{M}_s$ are square matrices of dimension S where the total number of degrees of freedom is $S=6(m_1+m_2+2)$.

3.2.2 Gear System Matrices

A three-dimensional dynamic model of helical gear pair is shown in Figure 19 will be employed here [3, 5]. The test gear pair is chosen as the example for this formulation formed by gears $t1$ and $t2$. Both gears are assumed to have rigid blanks that are connected to each other by a linear gear mesh spring $\bar{k}_t$ on the plane of action in the tooth normal direction determined by the helix angle β_t. Also applied in the same direction connected in series to $\bar{k}_t$ is a displacement excitation in the form motion transmission error $e_t(t)$. The relative positions of the gears are such that the line connecting the gear centers forms the positive x-axis of the coordinate frame. In this position, the plane of action makes an angle ψ_t with the positive y-axis as shown in Figure 19. As the plane of action changes direction depending on the direction of the loading, ψ_t is defined as

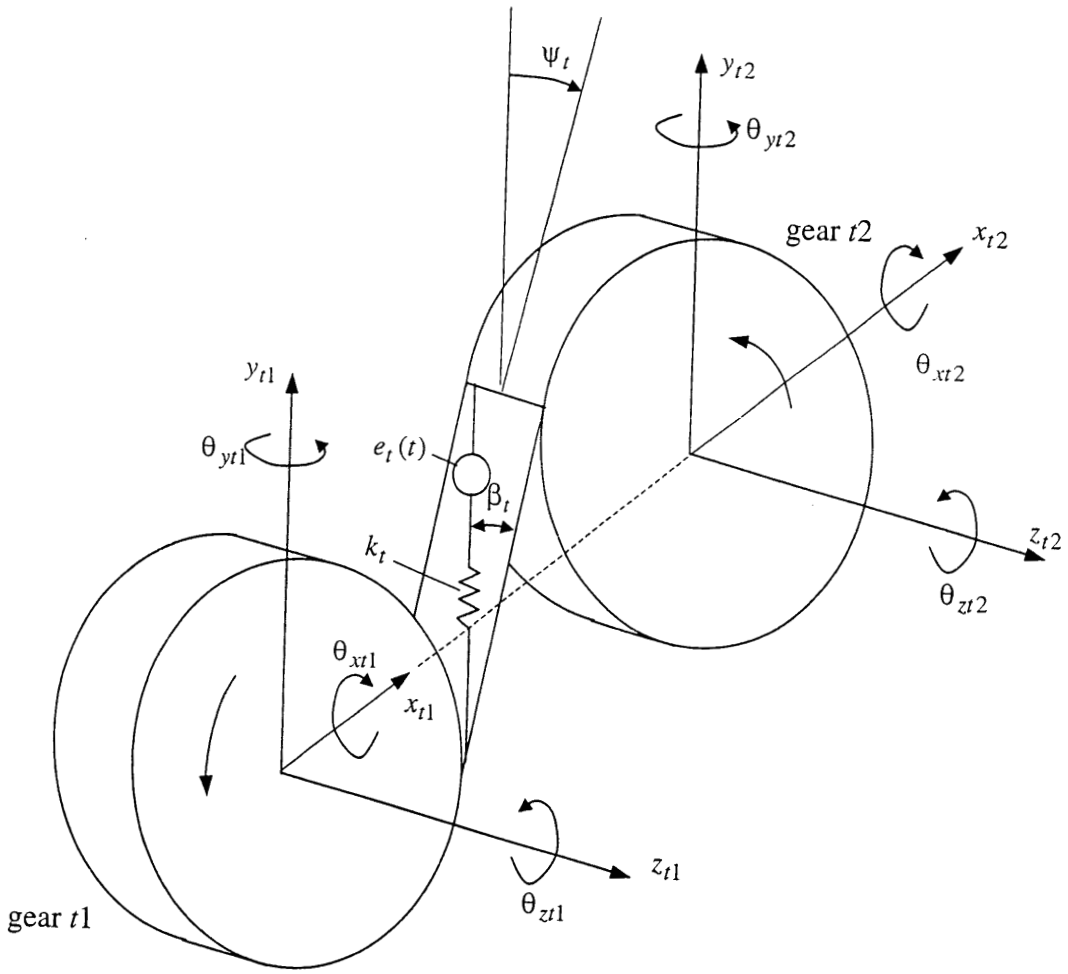

Figure 19. A 3D dynamic model of a helical gear pair [3, 5].

$$\psi_t = \begin{cases} \phi_t, & T_{t1} : counter\ clockwise \\ -\phi_t, & T_{t1} : clockwise \end{cases} \tag{15}$$

where ϕ_t is the transverse pressure angle of the gear pair and T_{t1} is the torque applied on the test gear $t1$. Helix angle β_t is defined based on the hand of the gear $t1$ as

$$\beta_t = \begin{cases} (+)ve & if\ \ gear\ t1\ has\ \ left\ hand\ \ teeth \\ (-)ve & if\ \ gear\ t1\ has\ \ right\ hand\ \ teeth \end{cases} \tag{16}$$

Both gears are allowed to translate in x and y directions in the transverse plane and in the axial z direction. In addition, each gear is allowed to rotate about these three axes by θ_x, θ_y and θ_z, respectively. Hence, with six degrees of freedom on each gear, the gear pair t has a total of 12 degrees of freedom that defines the coupling between the two shafts holding the gears. Equations of motion for gear $t1$ are given as:

$$m_{t1}\ddot{y}_{t1} + c_t \dot{p}_t(t) + \bar{k}_t p_t(t)\cos\beta_t \cos\psi_t = 0 \tag{17a-f}$$

$$m_{t1}\ddot{x}_{t1} + c_t \dot{p}_t(t) + \bar{k}_t p_t(t)\cos\beta_t \sin\psi_t = 0$$

$$m_{t1}\ddot{z}_{t1} - c_t \dot{p}_t(t) - \bar{k}_t p_t(t)\sin\beta_t = 0$$

$$I_{t1}\ddot{\theta}_{yt1} + r_{t1}c_t \dot{p}_t(t) + r_{t1}\bar{k}_t p_t(t)\sin\beta_t \cos\psi_t = 0$$

$$I_{t1}\ddot{\theta}_{xt1} + r_{t1}c_t \dot{p}_t(t) + r_{t1}\bar{k}_t p_t(t)\sin\beta_t \sin\psi_t = 0$$

$$J_{t1}\ddot{\theta}_{zt1} + r_{t1}c_t \dot{p}_t(t) + r_{t1}\bar{k}_t p_t(t)\cos\beta_t = T_{t1}$$

Equations of motion for gear $t2$:

$$m_{t2}\ddot{y}_{t2} - c_t \dot{p}_t(t) - \bar{k}_t p_t(t)\cos\beta_t \cos\psi_t = 0 \tag{18a-f}$$

$$m_{t2}\ddot{x}_{t2} - c_t \dot{p}_t(t) - \bar{k}_t p_t(t)\cos\beta_t \sin\psi_t = 0$$

$$m_{t2}\ddot{z}_{t2} + c_t \dot{p}_t(t) + \bar{k}_t p_t(t)\sin\beta_t = 0$$

$$I_{t2}\ddot{\theta}_{yt2} + r_{t2}c_t \dot{p}_t(t) + r_{t2}\bar{k}_t p_t(t)\sin\beta_t \cos\psi_t = 0$$

$$I_{t2}\ddot{\theta}_{xt2} + r_{t2}c_t\dot{p}_t(t) + r_{t2}\bar{k}_t p_t(t)\sin\beta_t \sin\psi_t = 0$$

$$J_{t2}\ddot{\theta}_{zt2} + r_{t2}c_t\dot{p}_t(t) + r_{t2}\bar{k}_t p_t(t)\cos\beta_t = -T_{t2}$$

In these equations, $p_t(t)$ represents the relative displacement at the test gear mesh in the direction normal to contact surfaces defined by

$$\begin{aligned} p_t(t) = &\left[(x_{t1} - x_{t2})\sin\psi_t + (y_{t1} - y_{t2})\cos\psi_t + r_{t1}\theta_{zt1} + r_{t2}\theta_{zt2}\right]\cos\beta_t \\ &+ \left[-z_{t1} + z_{t2} + (r_{t1}\theta_{xt1} + r_{t2}\theta_{xt2})\sin\psi_t + (r_{t1}\theta_{yt1} + r_{t2}\theta_{yt2})\cos\psi_t\right]\sin\beta_t - e_t(t) \end{aligned} \tag{19}$$

The stiffness coupling matrix and the mass matrix of the gear pair t are obtained from equations (17-19) as

$$\mathbf{k}_t = \begin{bmatrix} (\mathbf{k}_{11})_t & (\mathbf{k}_{12})_t \\ (\mathbf{k}_{21})_t & (\mathbf{k}_{22})_t \end{bmatrix}, \qquad \mathbf{M}_t = \begin{bmatrix} \mathbf{m}_{t1} & \mathbf{0} \\ \mathbf{0} & \mathbf{m}_{t2} \end{bmatrix} \tag{20, 21}$$

The corresponding displacement and alternating force vectors are given as

$$\mathbf{q}_t = \begin{Bmatrix} \mathbf{q}_{t1} \\ \mathbf{q}_{t2} \end{Bmatrix}, \qquad \mathbf{F}_t(t) = \begin{Bmatrix} (\mathbf{f}_1)_t \\ (\mathbf{f}_2)_t \end{Bmatrix} e_t(t) \tag{22, 23}$$

where $\mathbf{q}_{ti} = \begin{bmatrix} y_{ti} & x_{ti} & z_{ti} & \theta_{yti} & \theta_{xti} & \theta_{zti} \end{bmatrix}^T$ and $i = 1, 2$.

The above formulation can be repeated for the reaction gear pair formed by gears $r1$ (on the shaft 1) and $r2$ (on the shaft 2) to obtain the stiffness and mass matrices of the reaction gear pair as well by simply replacing the subscript t by subscript r in above equations with

$$\psi_r = \begin{cases} -\phi_r, & T_{t1} : counter\ clockwise \\ \phi_r, & T_{t1} : clockwise \end{cases} \tag{24}$$

$$\beta_r = \begin{cases} (+)ve & \text{if gear } r1 \text{ has left hand teeth} \\ (-)ve & \text{if gear } r1 \text{ has right hand teeth} \end{cases} \tag{25}$$

Accordingly, mass and stiffness matrices and the force and displacement vectors for the reaction gear pair are found to be:

$$\mathbf{k}_r = \begin{bmatrix} (\mathbf{k}_{11})_r & (\mathbf{k}_{12})_r \\ (\mathbf{k}_{21})_r & (\mathbf{k}_{22})_r \end{bmatrix}, \qquad \mathbf{M}_r = \begin{bmatrix} \mathbf{m}_{r1} & \mathbf{0} \\ \mathbf{0} & \mathbf{m}_{r2} \end{bmatrix}, \tag{26a,b}$$

$$\mathbf{q}_r = \begin{Bmatrix} \mathbf{q}_{r1} \\ \mathbf{q}_{r2} \end{Bmatrix}, \qquad \mathbf{F}_r(t) = \begin{Bmatrix} (\mathbf{f}_1)_r \\ (\mathbf{f}_2)_r \end{Bmatrix} e_r(t) \tag{27c,d}$$

The system shown in Figure 1 has a total of two shafts and four gears forming two gear pairs connecting certain degrees of freedom of each shaft to each other according to the formulation given above. The overall gear stiffness matrix and the mass matrix, both of dimension *S*, can be assembled in the form

$$\mathbf{K}_g = \begin{bmatrix} \ddots & & & & & & & \\ & (\mathbf{k}_{11})_t & & & & \textit{symm.} & & \\ & \vdots & \ddots & & & & & \\ & \mathbf{0} & \cdots & (\mathbf{k}_{11})_r & & & & \\ & \vdots & & \vdots & \ddots & & & \\ & (\mathbf{k}_{21})_t & \cdots & \mathbf{0} & \cdots & (\mathbf{k}_{22})_t & & \\ & \vdots & & \vdots & & \vdots & \ddots & \\ & \mathbf{0} & \cdots & (\mathbf{k}_{21})r & \cdots & \mathbf{0} & \cdots & (\mathbf{k}_{22})_r & \ddots \end{bmatrix} \tag{28}$$

$$\mathbf{M}_g = Diag\left[\cdots \quad \mathbf{m}_{t1} \quad \cdots \quad \mathbf{m}_{r1} \quad \cdots \quad \mathbf{m}_{t2} \quad \cdots \quad \mathbf{m}_{r2} \quad \cdots\right] \tag{29}$$

The masses and inertias of other non-gear components attached to a shaft must also be included in equation (22) at the appropriate nodes the same way the gear masses and inertias included.

3.2.3 Support Stiffness Matrices

In a typical application, each shaft is supported by least two rolling element bearings of varying type, size and design parameters. The most general way of describing flexibility of an individual bearing is to define a 6x6 stiffness matrix $\mathbf{k}_{bi}$ with zero torsional terms [3, 6]. If there are n_b number of bearings in the system, an overall bearing stiffness matrix of dimension S can be constructed by assembling the individual stiffness matrices according to the shaft node at which each bearing is mounted

$$\mathbf{K}_b = \begin{bmatrix} \ddots & & & & & \\ \mathbf{0} & \mathbf{k}_{b1} & & & \textit{symm.} & \\ \vdots & \vdots & \ddots & & & \\ \mathbf{0} & \mathbf{0} & \cdots & \mathbf{k}_{b2} & & \\ \vdots & \vdots & \cdots & \vdots & \ddots & \\ \mathbf{0} & \mathbf{0} & \cdots & \mathbf{0} & \cdots & \mathbf{k}_{bn_b} \end{bmatrix}. \tag{30}$$

3.2.4 Equations of Motion

Given the mass and stiffness matrices for shafts, bearings/case and gears, the overall mass and stiffness matrices of the overall system are given as

$$\mathbf{M} = \mathbf{M}_s + \mathbf{M}_g \tag{31}$$

$$\mathbf{K} = \mathbf{K}_s + \mathbf{K}_b + \mathbf{K}_g \tag{32}$$

Finally, the force vector is defined in terms of the two static transmission error excitations as

$$\mathbf{F}(t) = \begin{Bmatrix} \vdots \\ (\mathbf{f}_1)_t e_t(t) \\ \vdots \\ (\mathbf{f}_1)_r e_r(t) \\ \vdots \\ (\mathbf{f}_2)_t e_t(t) \\ \vdots \\ (\mathbf{f}_2)_r e_r(t) \\ \vdots \end{Bmatrix} \tag{33}$$

3.2.5 Natural Modes and Forced Response

Equations of motion of the overall system can be written in matrix form as

$$\mathbf{M}\,\ddot{\mathbf{X}}(t) + \mathbf{C}\,\dot{\mathbf{X}}(t) + \mathbf{K}\,\mathbf{X}(t) = \mathbf{F}(t) \tag{34}$$

The transverse-torsional model formulation presented up to this point did not include the derivation of the damping matrix **C**. If the damping values of each component including gear meshes, bearings and shafts were known, one could obtain a damping matrix that is in the same form as **K**. However, these damping values are not known in most cases. Therefore, here for practical engineering purposes, a set of modal damping values ζ_i are used to define **C** instead of using a damping matrix that is formed by actual damping values.

The eigen value problem governing equation (34) yield the natural frequencies ω_i and the corresponding modal vectors Φ_i (mode shapes) where $i = 1, 2, \ldots, S$ is the modal index. The Sequential Jacobi Method is used here for the Eigen Value solutions as in the case of the torsional model. The forced response of the system is obtained by using the same approach (Modal Summation Technique) as the torsional model, now with the forcing vector given by equation (25) where $e_t(t)$ and $e_r(t)$ are defined by equations (4) and (5), respectively.

4. Parametric Studies and Design Recommendations

4.1 Dynamic Behavior of the Current Test Rig

As the first application of the dynamic models, the current NASA GRC gear durability test machine is simulated. The system parameters of the test rig required by the dynamic models are listed in Table 3. While the torsional model of Figure 17 has only four degrees of freedom (DOF), the 3D model shown in Figure 20 has 246 DOF.

The dynamic forces at the test gear mesh are of particular interest here since the durability of the test gear is heavily dependent on the load the gear mesh experiences. The static transmission error excitation amplitudes predicted by the contact mechanics models $\tilde{e}_{ti}$ and $\tilde{e}_{ri}$ listed in Table 2 are used in this simulation. In addition, indexing error amplitudes of $E_{r1} = E_{r2} = 10\,\mu m$ are used as a representative value of the measured errors, and a 5 percent damping value is considered.

Torsional and 3D model predictions of are compared in Figure 21 for the case when the test gear set has no face offset and no reaction gear index errors $E_{r1} = E_{r2} = 0$. The vertical axis represents maximum alternating force amplitude of the test gear mesh F_{ta} and the horizontal axis is the shaft speed in rpm. The same is presented in Figure 22 when the test gears are offset in the face direction as described earlier. In both figures, the predictions from both models are in reasonably good agreement. The differences are simply due to the factors that cannot be included in the purely torsional model. Comparison of torsional predictions for cases with and without offset shown in Figure 23 indicate that F_{ta} are much lower when there is face off-set.

One major observation from Figure 21 to 23 is that regardless of the model used or face off-set condition considered, the current test condition [7] of 10,000 rpm shaft speed is in close vicinity of last to natural frequencies, and hence, it is close to the primary resonance peaks. This suggests that the current test condition involves a significant amount of dynamic gear mesh forces in addition to the static force transmitted. Also observed from these figures that a minor change in the operating speed condition in either direction or a minor structural change to the test machine to change the

Table 3

System parameters of the NASA gear durability test machine

	mass (kg)	inertia (kg-m^2)	mesh stiffness (N/m)
Test gear	0.407	3.57×10^{-4}	8.57×10^{7}
Reaction gear with hydraulic unit	2.41	2.42×10^{-3}	6.18×10^{8}
Reaction gear without hydraulic unit	3.01	2.82×10^{-3}	6.18×10^{8}

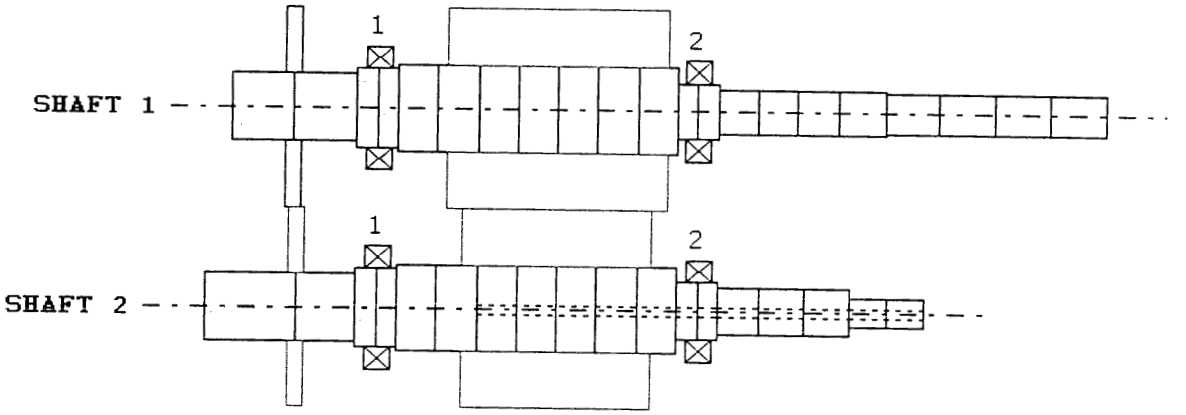

Figure 20. 3D dynamic model of the NASA gear durability test rig.

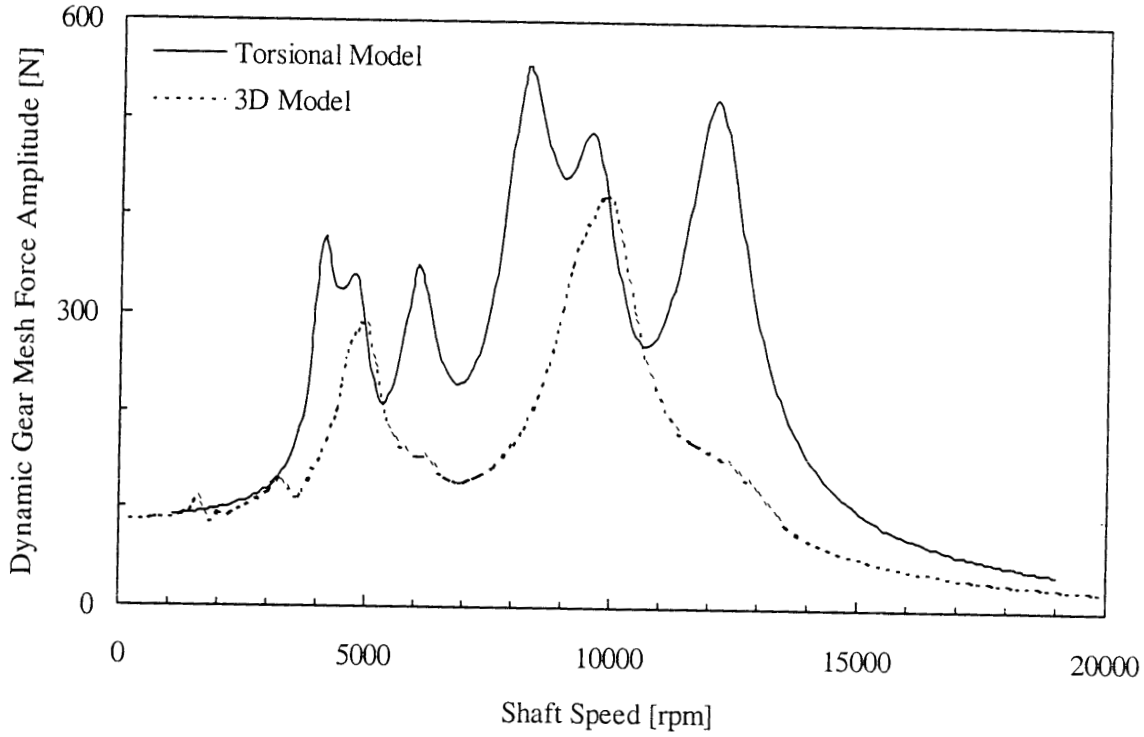

Figure 21. Dynamic force amplitude of the test gear pair as a function of shaft speed when there is no test gear face offset. $\tilde{e}_{t1} = 0.56\ \mu m$, $\tilde{e}_{t2} = 0.30\ \mu m$, $\tilde{e}_{r1} = 0.67\ \mu m$, $\tilde{e}_{r2} = 0.42 \mu m$, and $E_{r1} = E_{r2} = 0$.

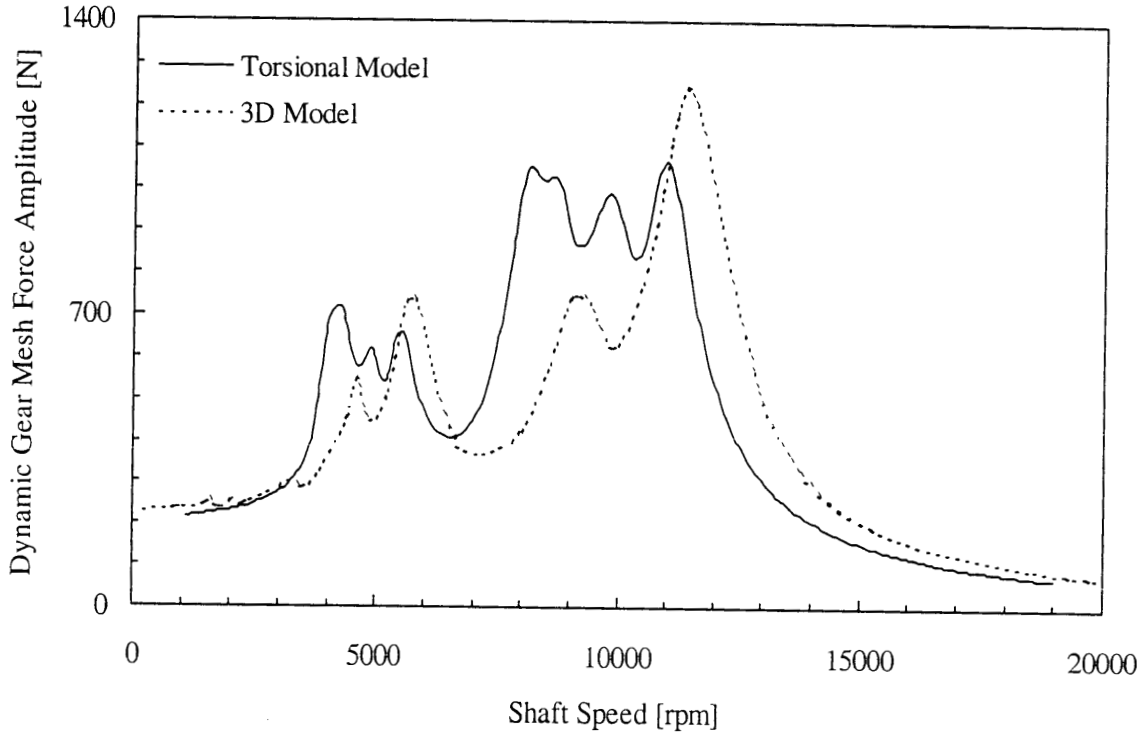

Figure 22. Dynamic force amplitude of the test gear pair as a function of shaft speed when there is test gear face offset. $\tilde{e}_{t1} = 2.26\ \mu m$, $\tilde{e}_{t2} = 1.11\ \mu m$, $\tilde{e}_{r1} = 0.67\ \mu m$, $\tilde{e}_{r2} = 0.42 \mu m$, and $E_{r1} = E_{r2} = 0$.

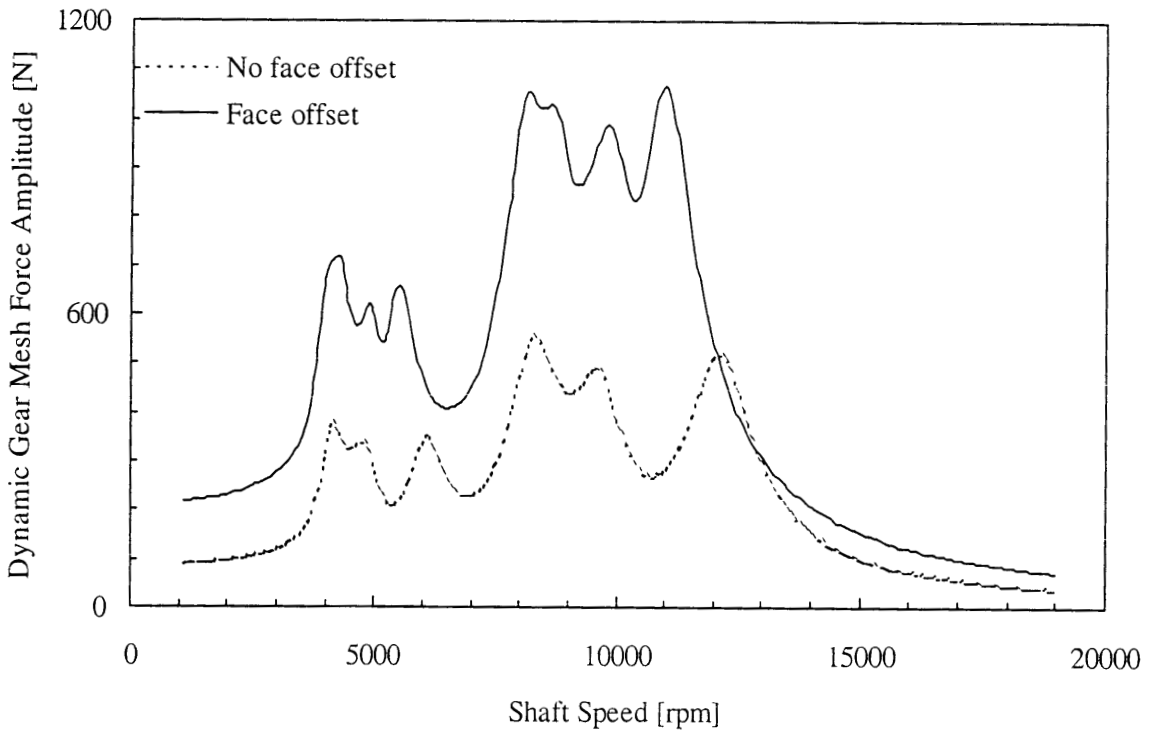

Figure 23. Comparison of test gear mesh dynamic force amplitudes for cases with and without face offset for $E_{r1} = E_{r2} = 0$, $\tilde{e}_{r1} = 0.67\ \mu m$ and $\tilde{e}_{r2} = 0.42 \mu m$. $\tilde{e}_{t1} = 2.26\ \mu m$ and $\tilde{e}_{t2} = 1.11\ \mu m$ for the case of face offset, and $\tilde{e}_{t1} = 0.56\ \mu m$ and $\tilde{e}_{t2} = 0.30\ \mu m$ for the case no face offset.

natural frequencies would not be sufficient to move the operating speed away from the regions of resonance

4.2 Vibration Transmission-Isolation Characteristics of the Current Test Rig

The next item investigated is the issue of force and vibration transmissibility. Ideally, the disturbances originated at the reaction gear pair should be prevented from traveling to the test side to alter the test conditions, especially gear mesh load. As the only paths of the vibration transfer, the connecting shafts become the focus of such an investigation. These shafts on the current machine are rather short and have a reasonably large diameter ($L_{current} = 112\,mm$ and $d_{current} = 34\,mm$) resulting in a relatively high torsional stiffness value ($k_{s1} = k_{s2} = 9.8 \times 10^4 \quad Nm/rad$).

In order to quantify the amount of dynamic gear mesh force caused by the disturbances of the reaction gear mesh, a number of limiting cases are considered. In the first case shown in Figure 24, only the gear mesh component of the transmission error of the reaction gear pair $e_r(t)$ are included in the simulation ($e_t(t) = 0$, $E_{r1} = E_{r2} = 0$) and test gear mesh dynamic load amplitude F_{ta} that is solely due to $e_r(t)$ is plotted as a function of the shaft speed. Figure 24 indicates a major resonance peak at 8,000 rpm exited completely by $e_r(t)$ causing F_{ta} to reach high values. This suggests that the current test rig, especially its shafts, is not effective in isolating the reaction gear pair. Next, in addition to $e_r(t)$, once-per-revolution errors of the reaction gears are also included in the analysis. A representative value for each gear is considered $E_{r1} = E_{r2} = 10\,\mu m$ with $e_t(t) = 0$. Figure 25 shows F_{ta} as a function of the shaft speed given the relative reaction gear position angles $\gamma_{r2} - \gamma_{r1} = 180°$. Here, the shape the curve in Figure 24 is maintained except it is shifted upward by more than 300 N. In this figure, the resonance peaks are still due to $e_r(t)$ while this overall shift is caused by the indexing errors E_{r1} and E_{r2}.

The total F_{ta} due to all three excitations $e_t(t)$, $e_r(t)$ and $E_{r1} = E_{r2}$ is shown in Figure 26 for three different relative reaction gear position angles $\gamma_{r2} - \gamma_{r1} = 0, 90°, 180°$. This figure compared to Figure 22 suggests that the influence of $E_{r1} = E_{r2}$ is eliminated when $\gamma_{r2} - \gamma_{r1} = 0$, in order words, when the orientation of the high points of the indexing errors are made the same in assembly.

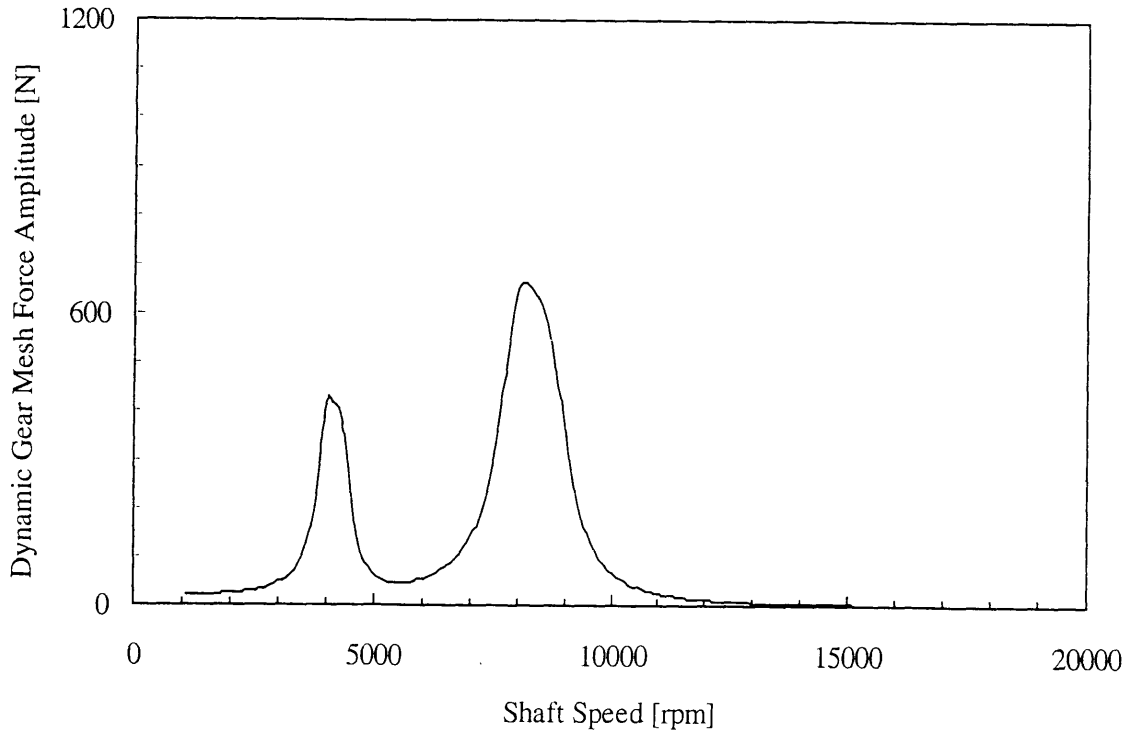

Figure 24. Dynamic force amplitude of the test gear pair with face offset due to the $e_r(t)$ given $e_t(t) = 0$ and $E_{r1} = E_{r2} = 0$. $\tilde{e}_{r1} = 0.67\ \mu m$ and $\tilde{e}_{r2} = 0.42 \mu m$.

Therefore, the alternating force time history $F_t(t)$ at 10,000 rpm shown in Figure 27(a) for $\gamma_{r2} - \gamma_{r1} = 0$ has a variation at each test gear mesh cycle only. The time history in Figure 27(b) for $\gamma_{r2} - \gamma_{r1} = 90^\circ$ contains both mesh and shaft components superimposed on each other. The once-per mesh variations are caused by $e_t(t)$ and $e_r(t)$ while the once-per-revolution variation comes from $E_{r1} = E_{r2}$. Finally, in Figure 27(c) for $\gamma_{r2} - \gamma_{r1} = 180^\circ$ (indexing errors are 180 degrees out of phase), the once-per-revolution variations of $F_t(t)$ are the most severe causing a significant chance of dynamic loading from tooth to tooth of the test gears. For instance, in Figure 27(c), seventh tooth of the test gears has only $F_{ta} \approx 500\ N$ while the 21th tooth that is 180 degrees from the seventh tooth has a maximum value of $F_{ta} \approx 1250\ N$.

To further investigate this issue of unequal loading on each tooth, a large number of test gears from a previous study [8] that were run to failure were inspected on the gear CMM. A 100 percent inspection of each tooth were done and wear amounts on each profile were quantified as illustrated in Figure 28 for one of the test gears. As the wear amounts are proportional to the load applied [9], any unequal wear amounts would confirm the results of the dynamic model. The maximum wear amounts on each tooth of this test gear is plotted in Figure 29. This figure shows a sinusoidal variation of wear amounts from tooth to tooth reaching a maximum value of more than 150 μm at tooth-12 while the wear amounts are negligible at the opposite side of the gear. Three-dimensional wear profiles of Figure 30 for four of the teeth (the ones marked with an arrow in Figure 29) offer further evidence that the once-per-revolution errors of the reaction gears were indeed not isolated to cause undesirable loading conditions.

4.3 Design Parameter Studies

Two main parameters were varied to observe their influence of the dynamic behavior of the test rig. These parameters are the length L and diameter d of the connecting shafts. The values of these parameters were varied around the current values and the resultant changes in the dynamic behavior were recorded. Influence of L on the torsional natural frequencies ω_i is shown in Figure 31. Here ω_3 and ω_4 are of special interest as all of the resonance peaks in forced response curves are

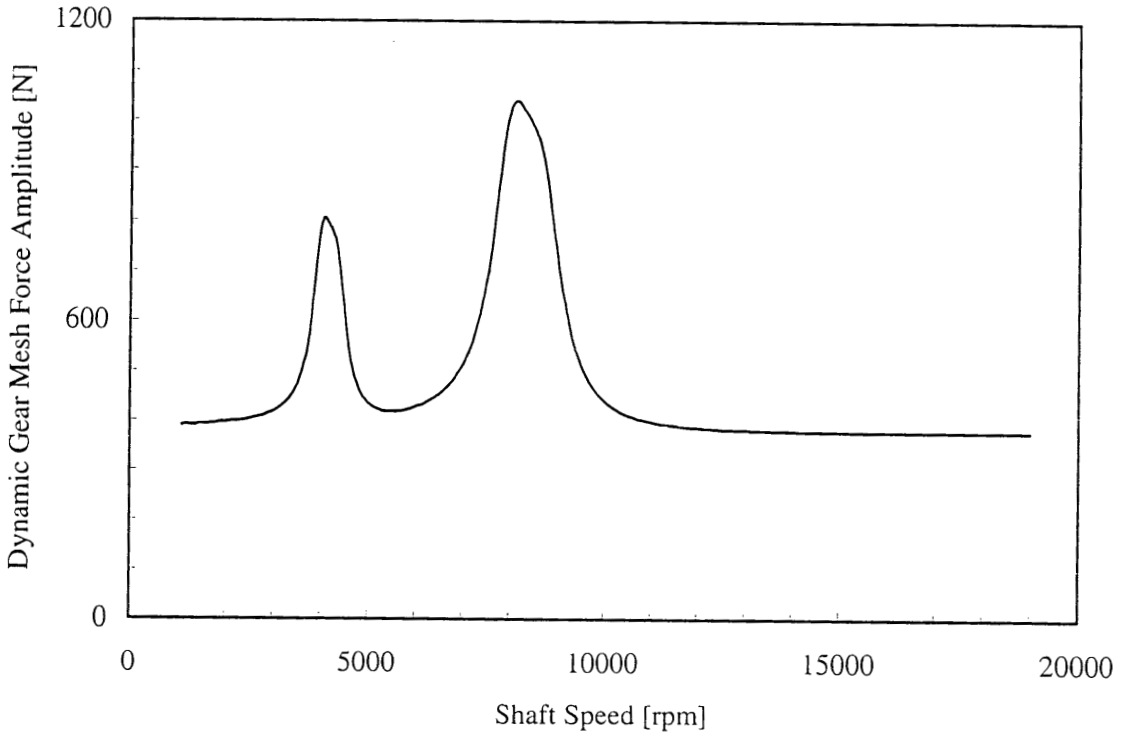

Figure 25. Dynamic force amplitude of the test gear pair with face offset due to the $e_r(t)$ given $e_t(t) = 0$, $E_{r1} = E_{r2} = 10\ \mu m$ and $\gamma_{r2} - \gamma_{r1} = \pi$. $\tilde{e}_{r1} = 0.67\ \mu m$ and $\tilde{e}_{r2} = 0.42 \mu m$.

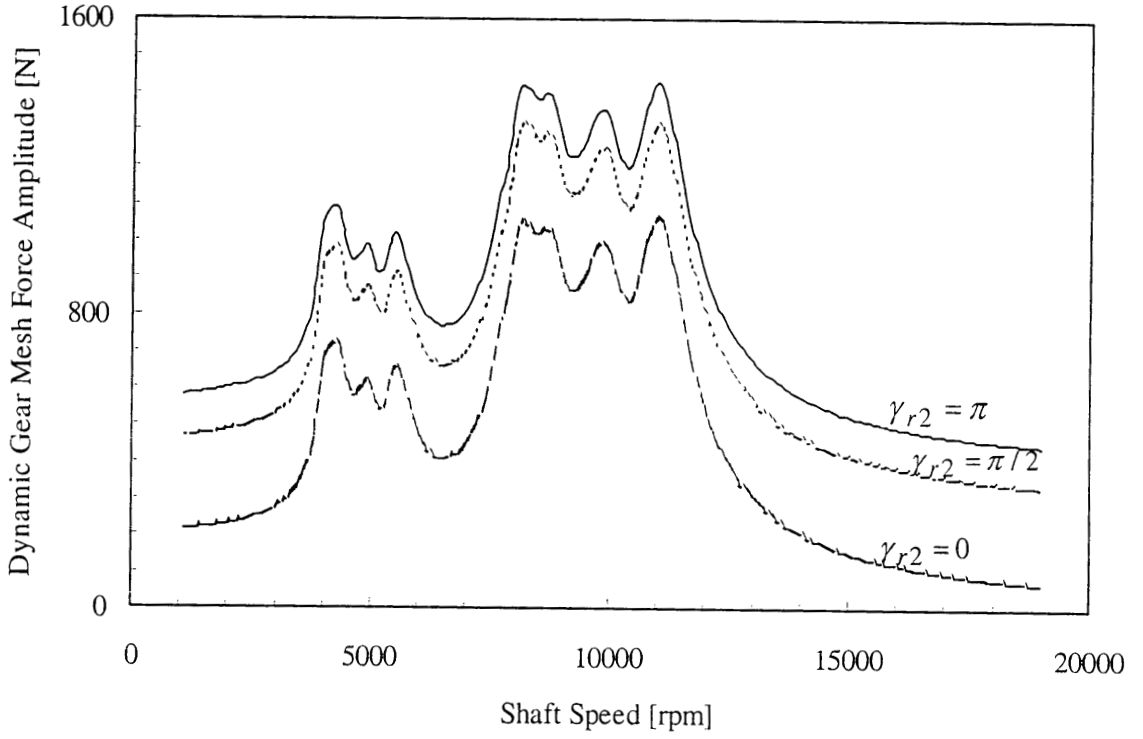

Figure 26 Influence of reaction gear phase angles on dynamic force amplitude of the test gear pair for the case with face offset. $\tilde{e}_{t1} = 2.26\,\mu m$, $\tilde{e}_{t2} = 1.11\,\mu m$, $\tilde{e}_{r1} = 0.67\,\mu m$ $\tilde{e}_{r2} = 0.42\mu m$, $E_{r1} = E_{r2} = 10\mu m$, $\gamma_{r1} = 0$, and $\gamma_{r2} = 0, \pi/2, \pi$.

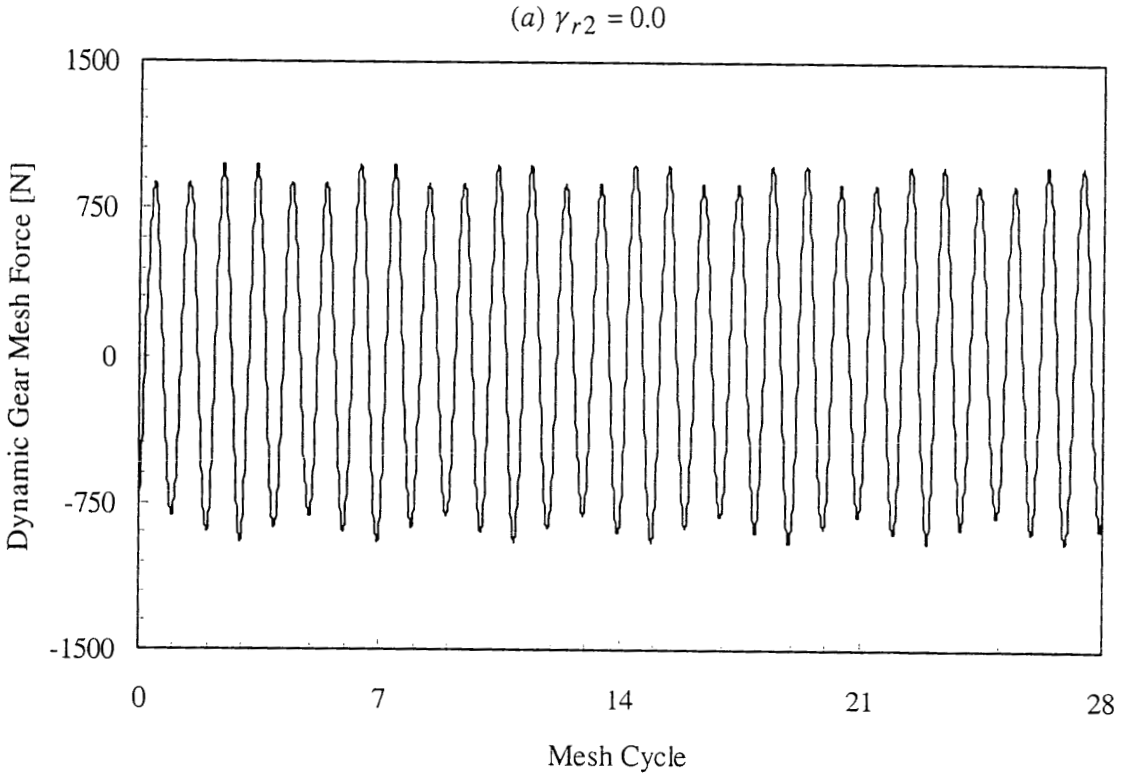

Figure 27. Dynamic force time history of the test gear pair with face offset at 10,000 *rpm* shaft speed. $\tilde{e}_{t1} = 2.26\ \mu m$, $\tilde{e}_{t2} = 1.11\ \mu m$, $\tilde{e}_{r1} = 0.67\ \mu m$ $\tilde{e}_{r2} = 0.42\ \mu m$, $E_{r1} = E_{r2} = 10\ \mu m$, $\gamma_{r1} = 0$. (a) $\gamma_{r2} = 0$, (b) $\gamma_{r2} = \pi/2$, and (c) $\gamma_{r2} = \pi$.

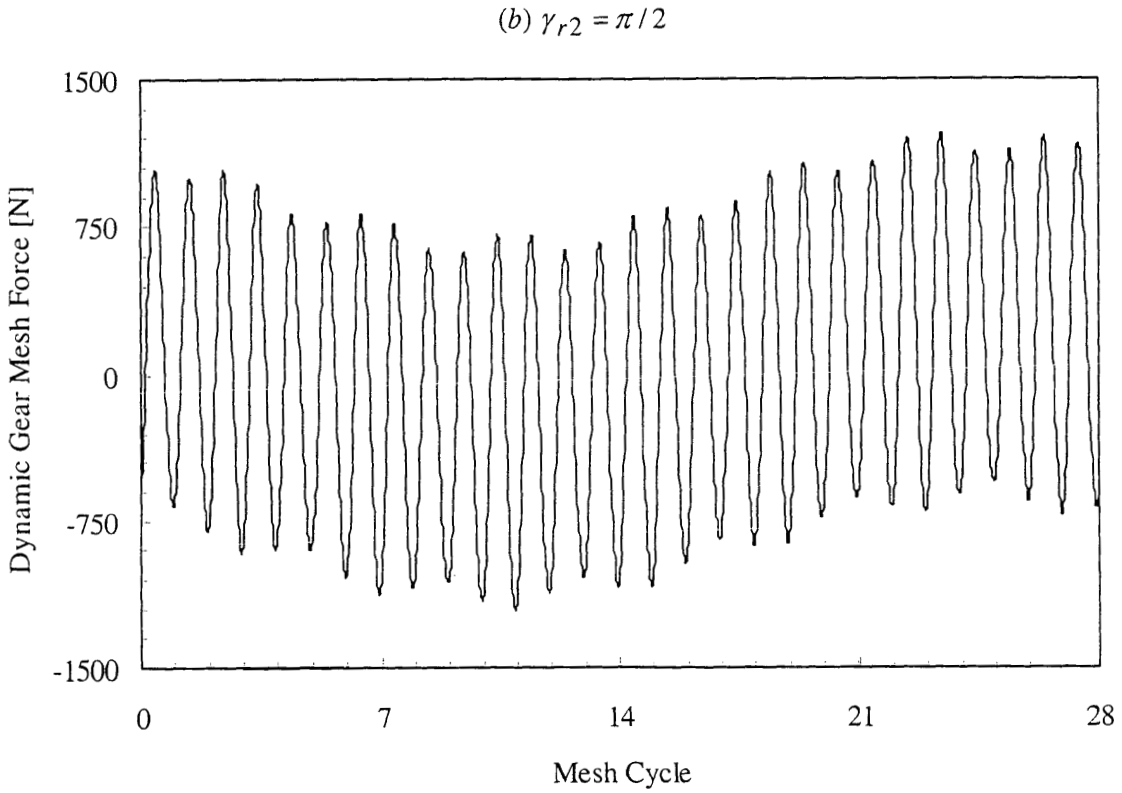

Figure 27. Continued.

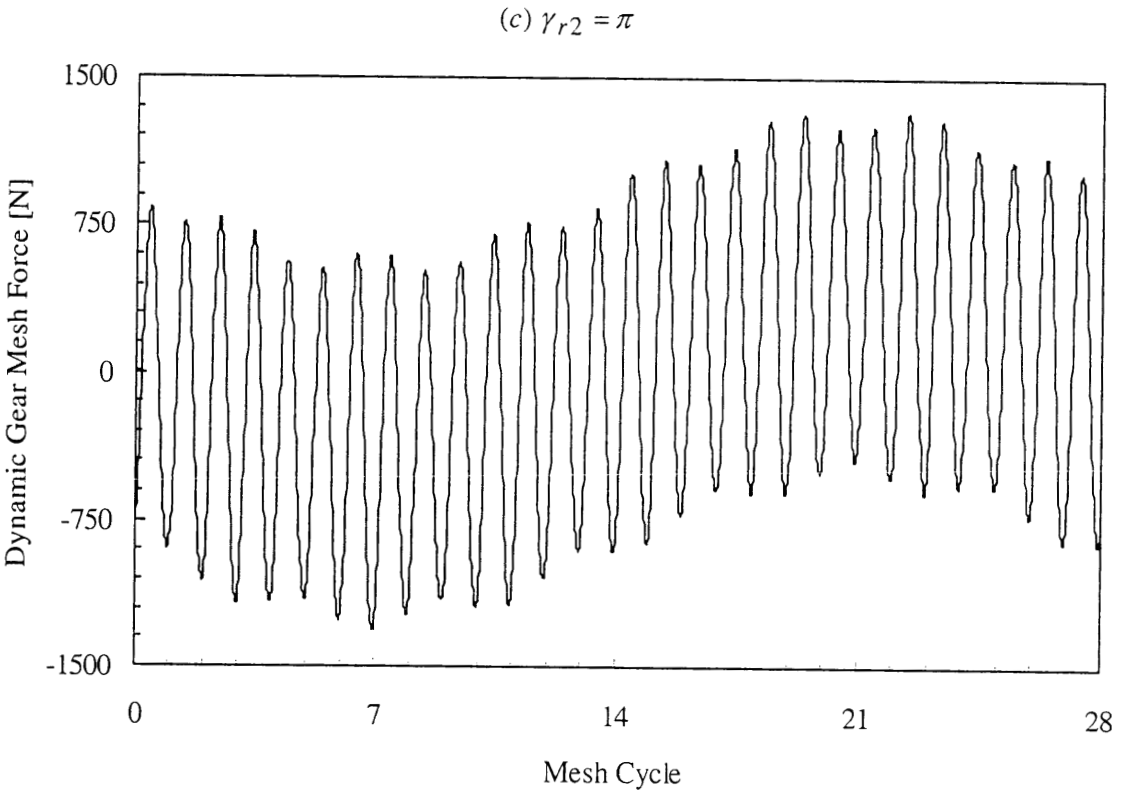

Figure 27. Continued.

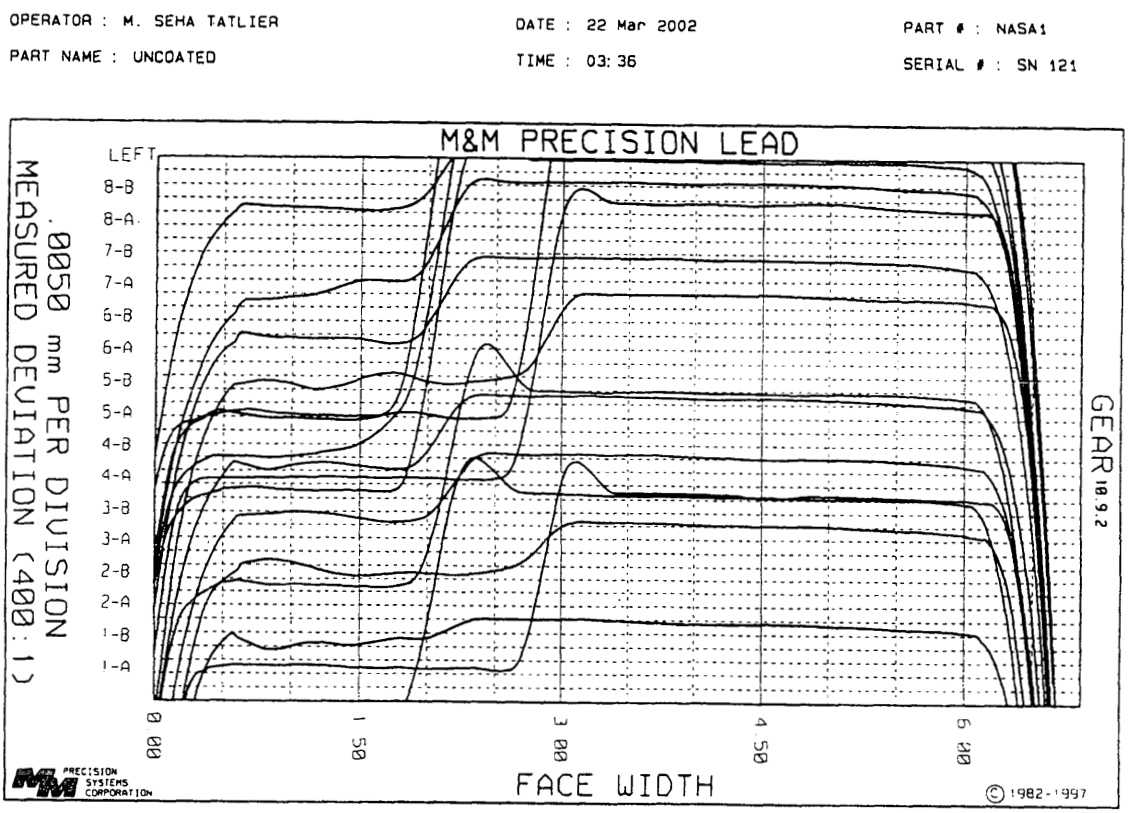

Figure 28. CMM inspection of a failed test gear.

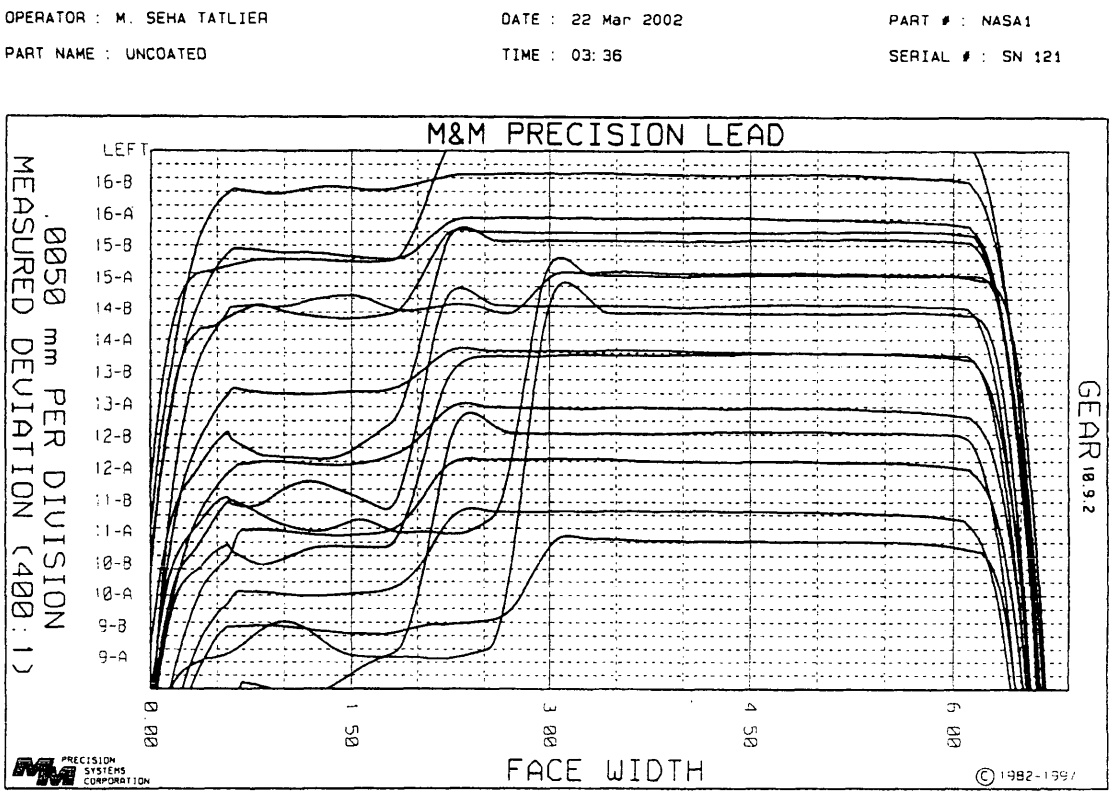

Figure 28. Continued.

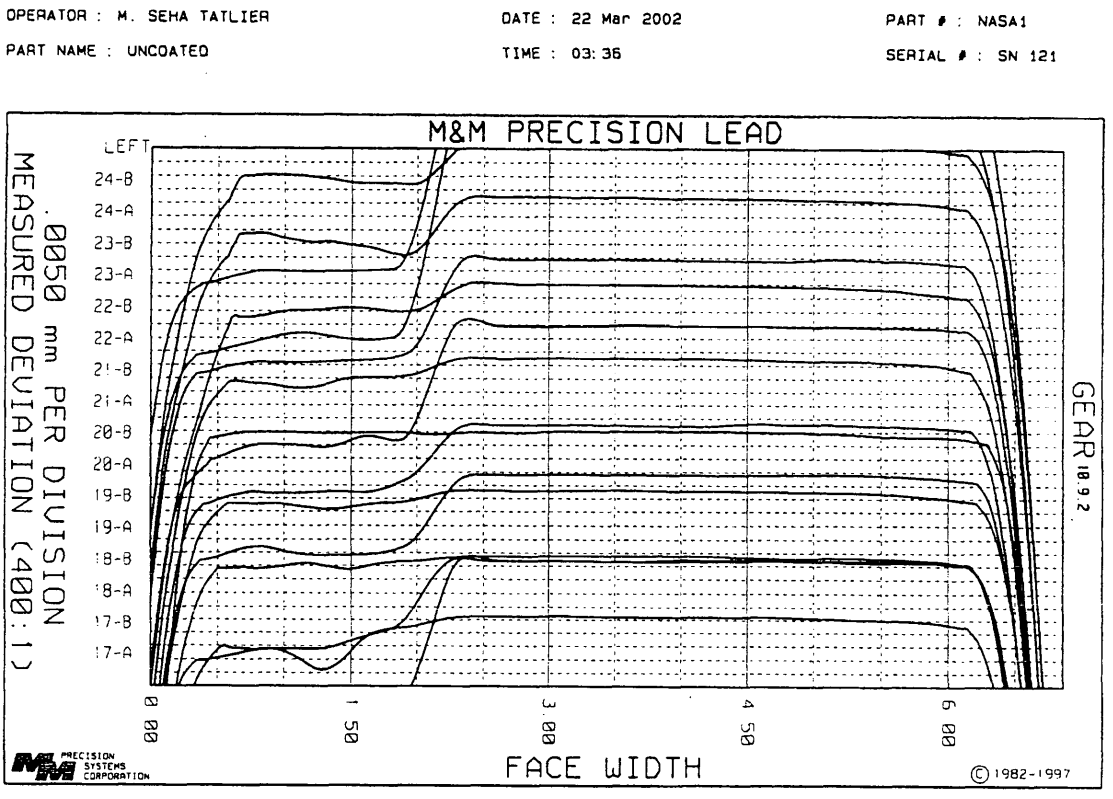

Figure 28. Continued.

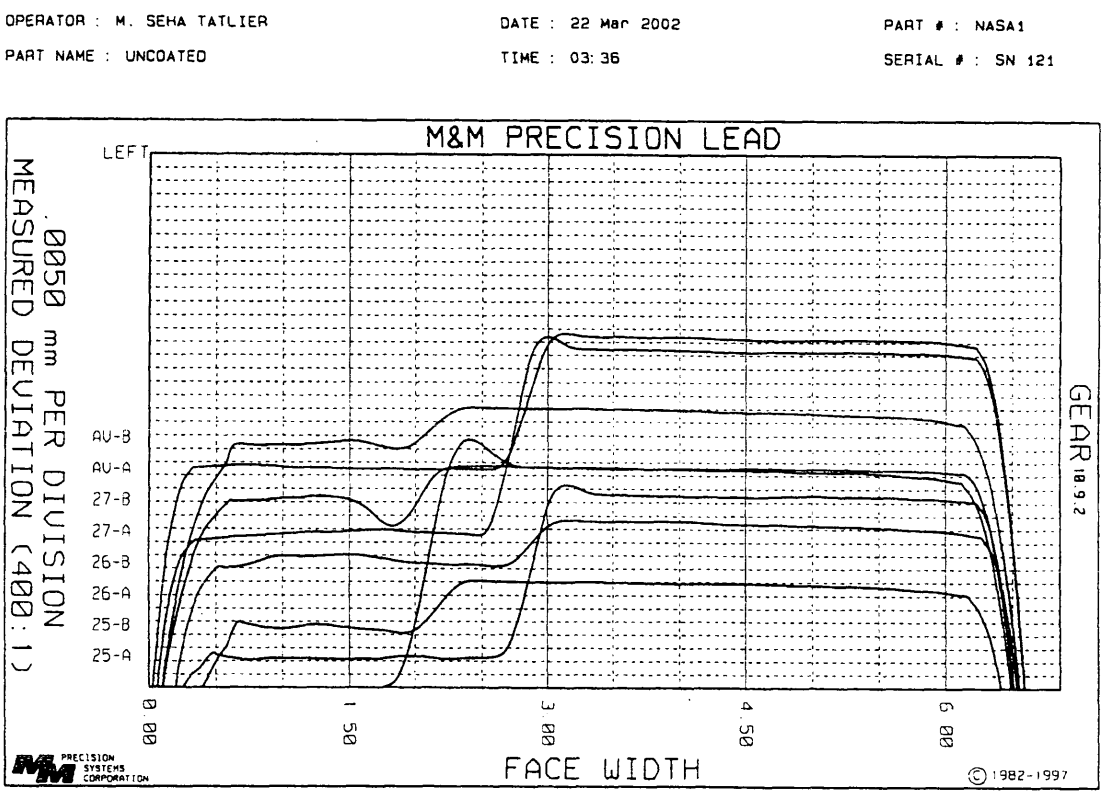

Figure 28. Continued.

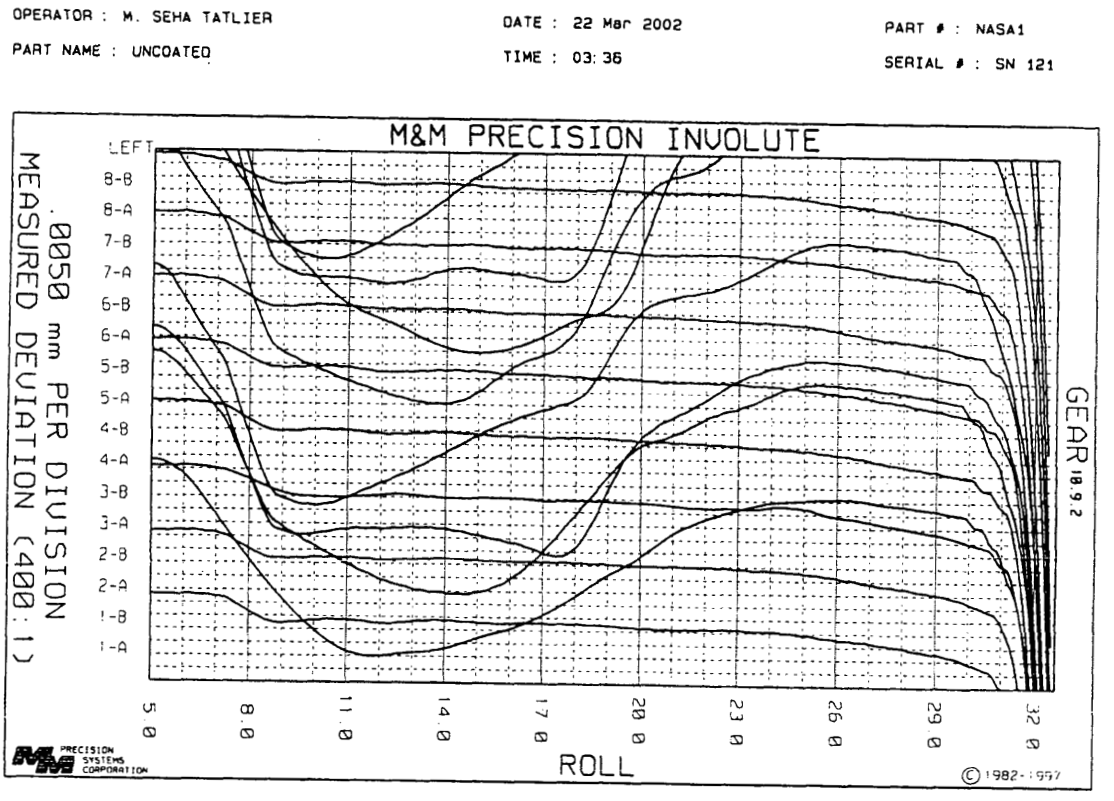

Figure 28. Continued.

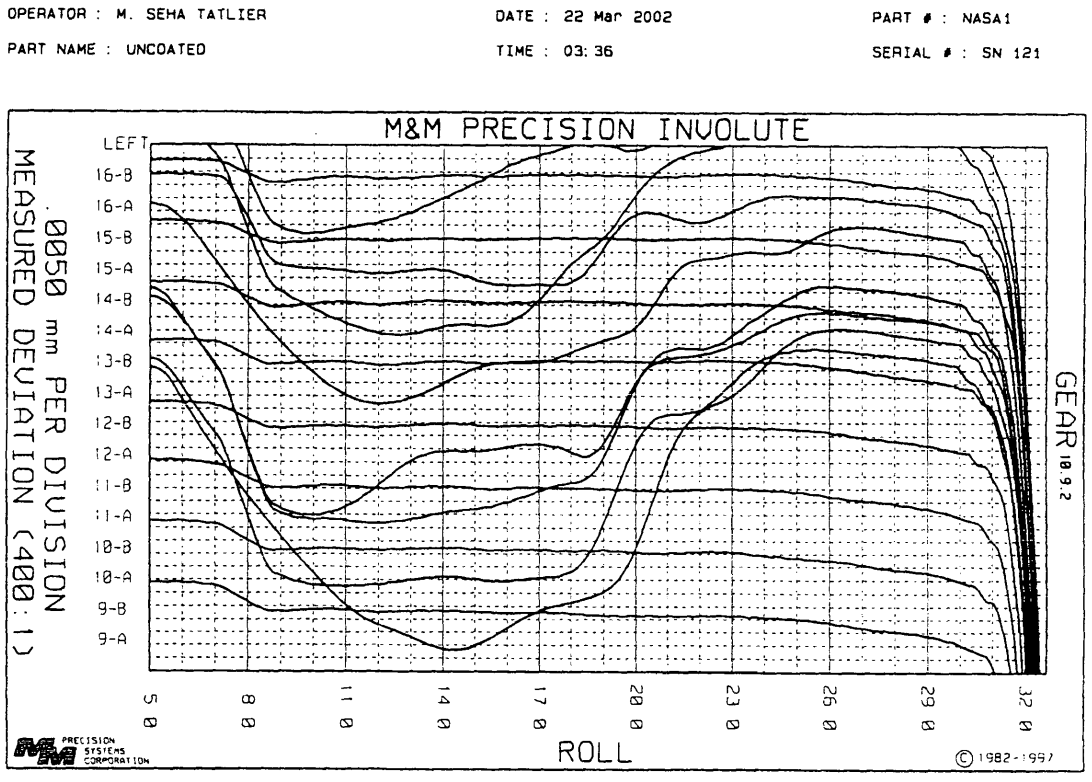

Figure 28. Continued.

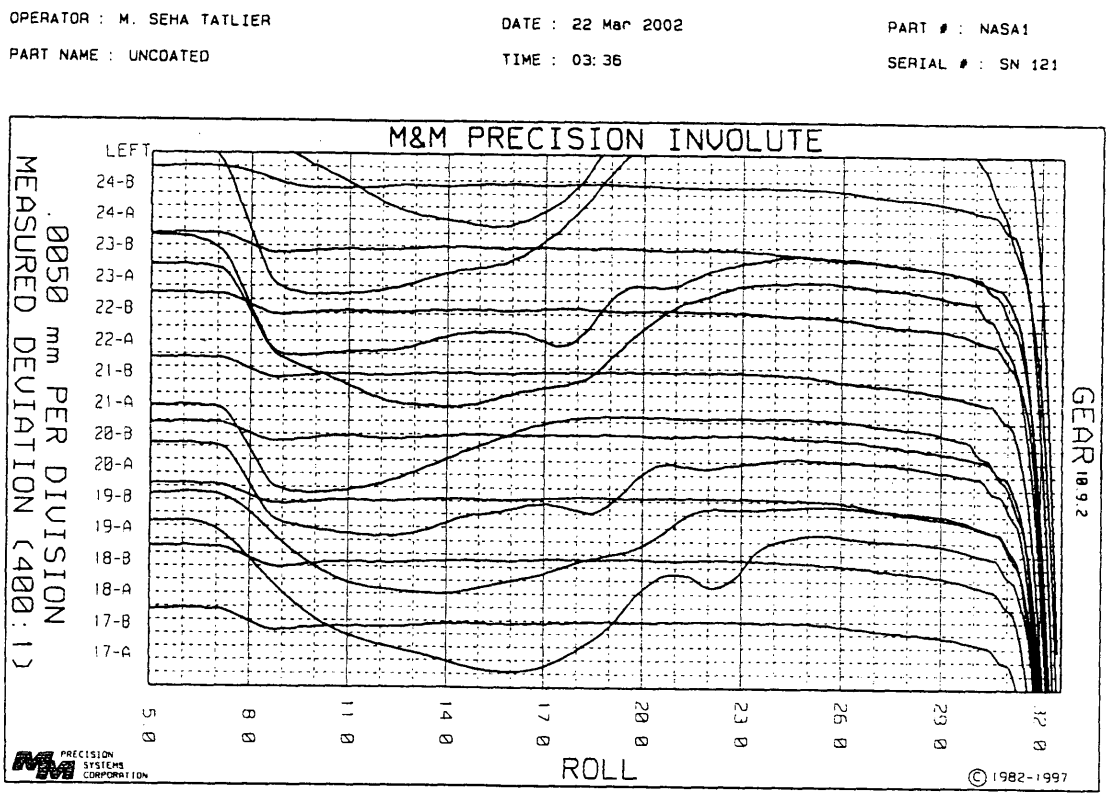

Figure 28. Continued.

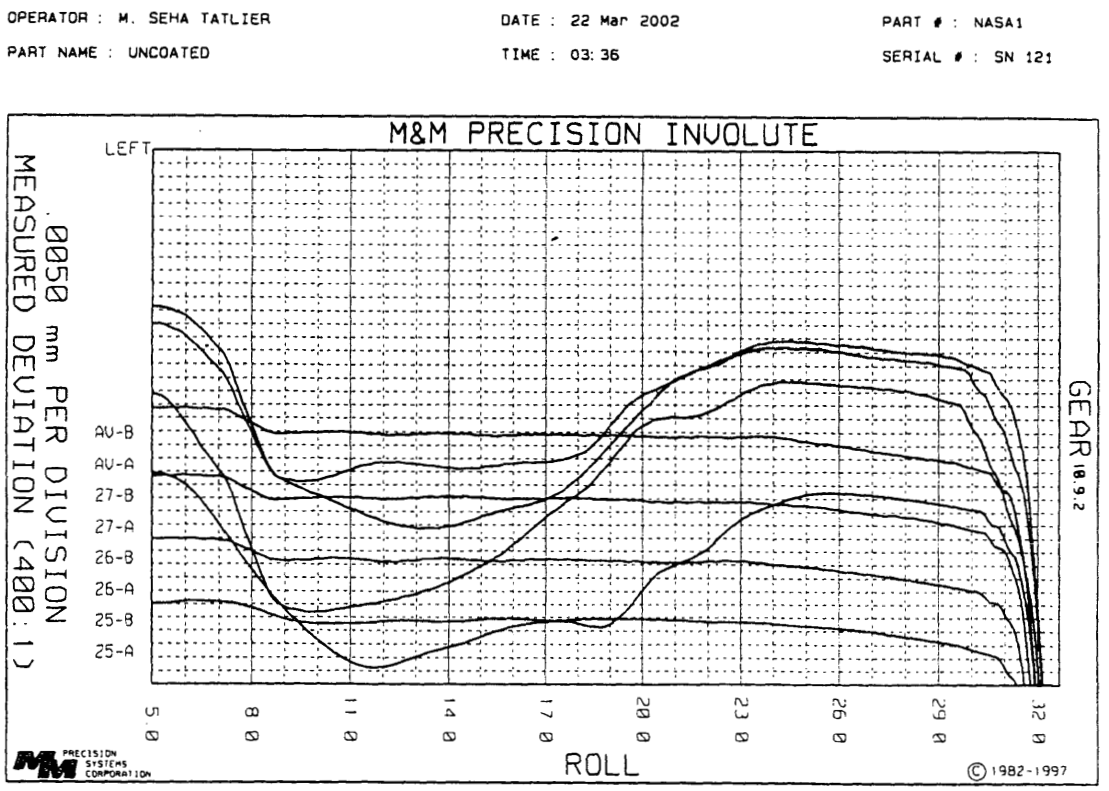

Figure 28. Continued.

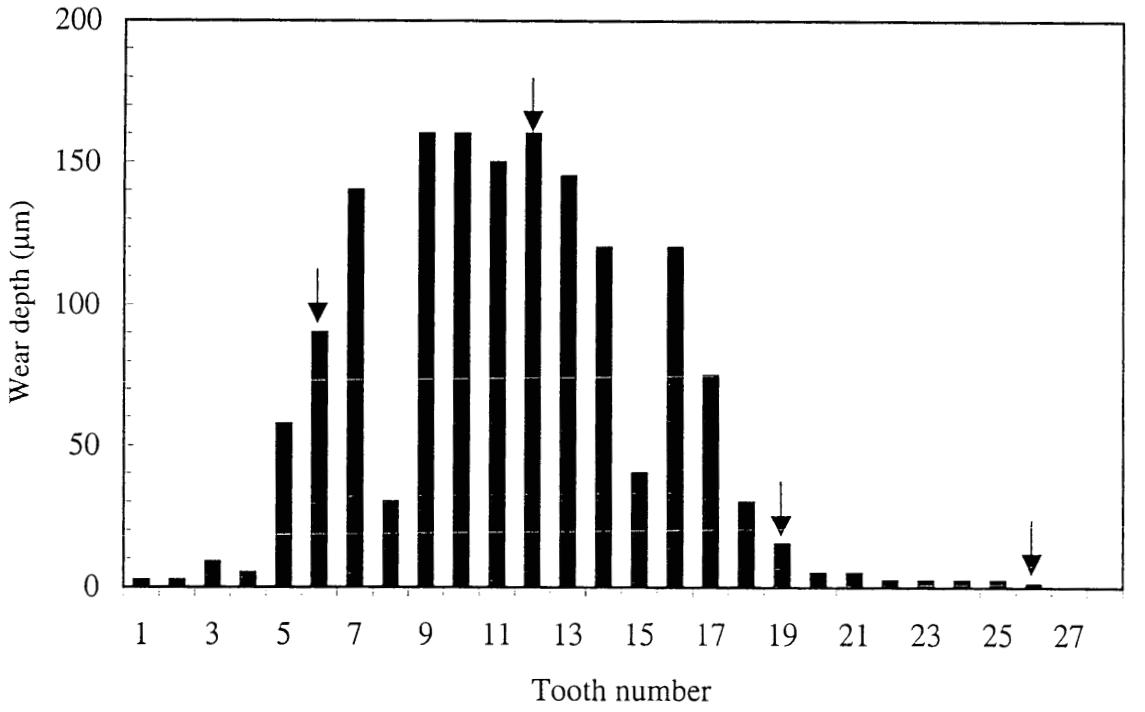

Figure 29. Measured wear depths of a test gear as a function of tooth number.

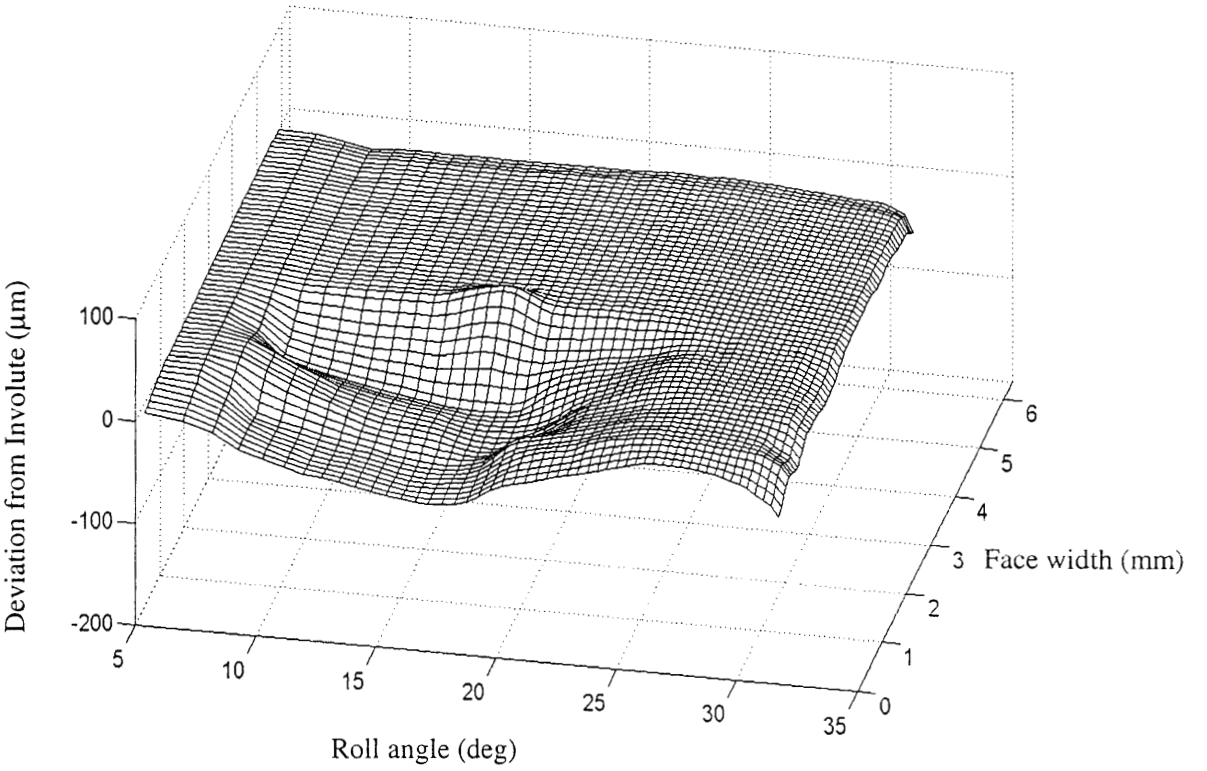

(a)

Figure 30. 3D tooth surface inspection of the test gear of Figure 29; (a) tooth #6, (b) tooth #12, (c) tooth #19, and (d) tooth #26.

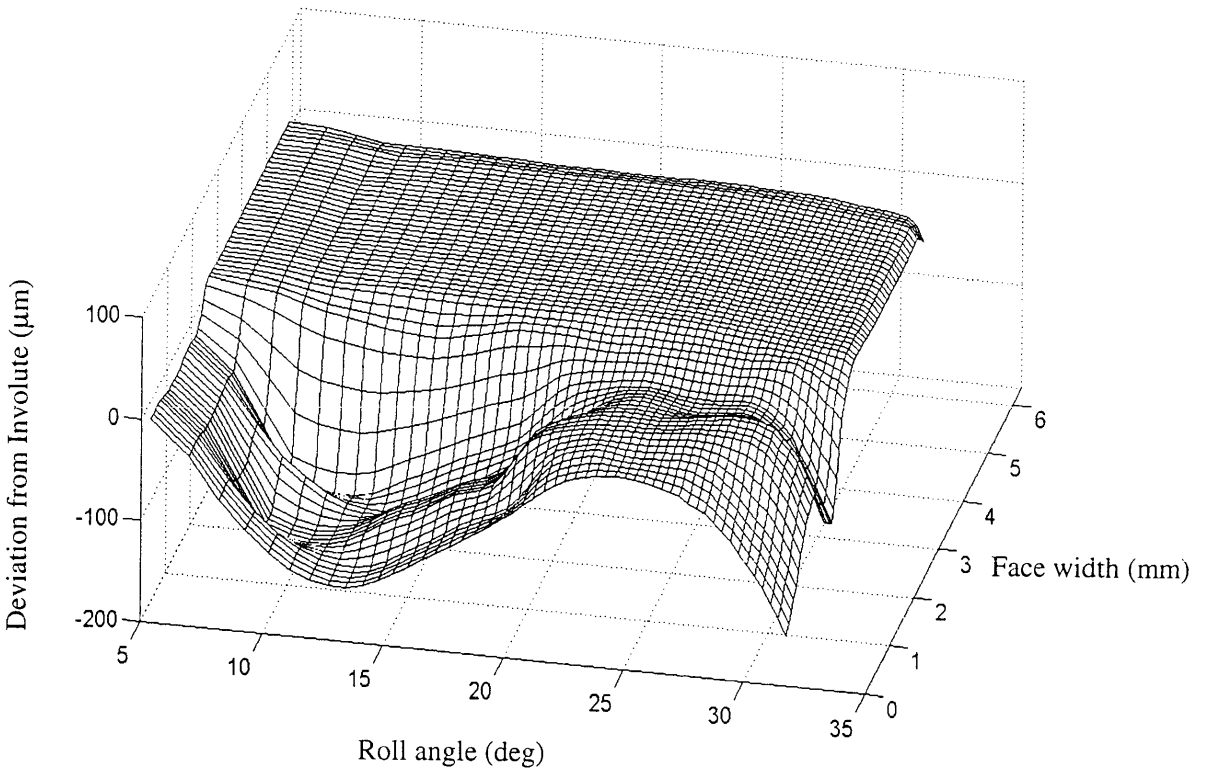

(b)

Figure 30. Continued

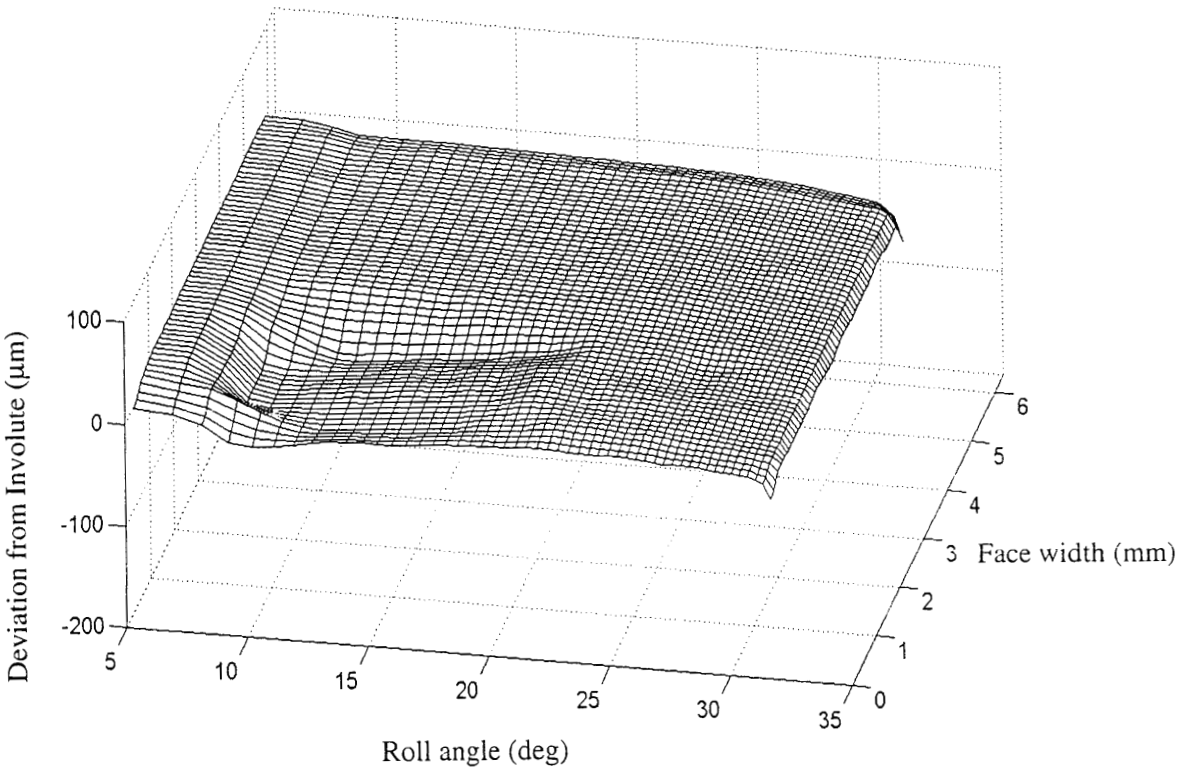

(c)

Figure 30. Continued.

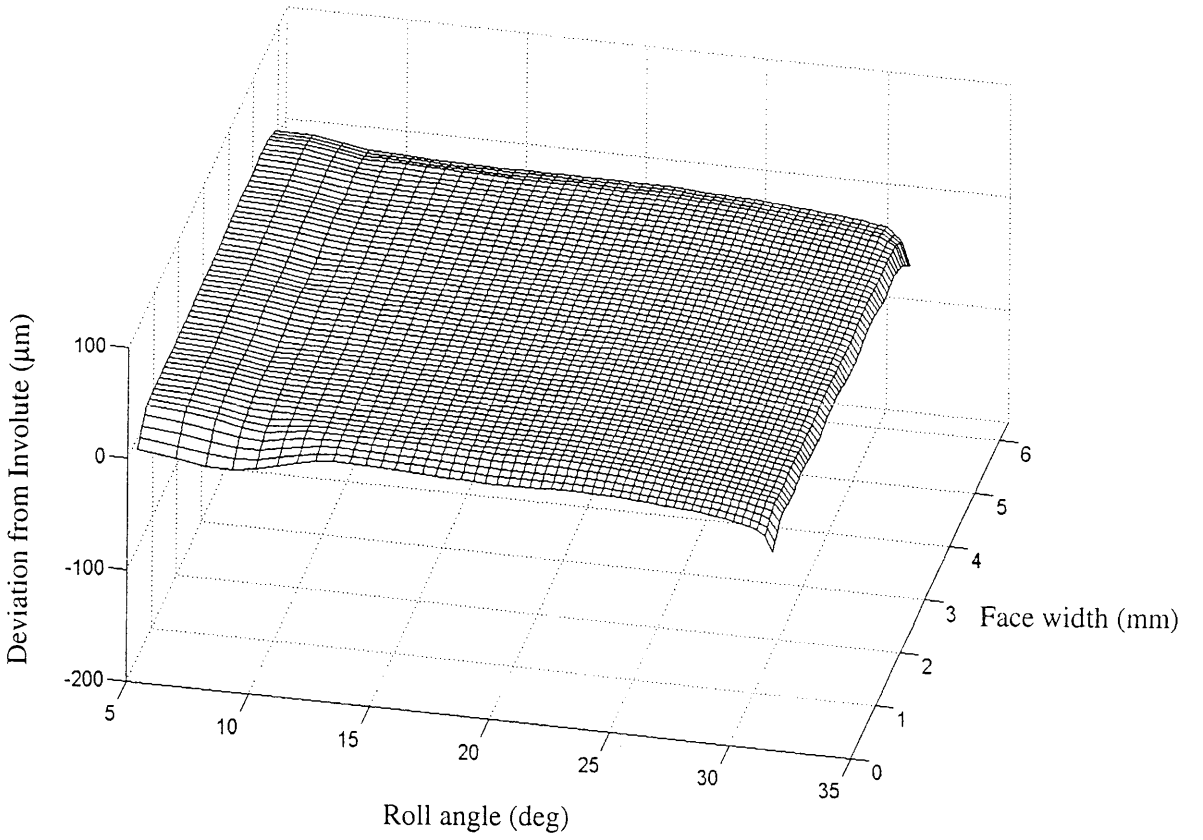

(d)

Figure 30. Continued.

associated with these two modes. As shown in this figure, both ω_2 and ω_4 are reduced as L is increased. We note that $\omega_4 = 4800\ Hz$ for $L/L_{current} > 2$ remaining unchanged with L. Considering that the mesh frequency at 10,000 rpm is $f_t = (10{,}000)(28)/60 = 4{,}666\ Hz$, an increase in L will not completely eliminate the resonances near the operating speed while moving them to the right by a certain amount as shown in Figure 32 for $L/L_{current} = 1, 3$ and 5. In this figure $\gamma_{r2} - \gamma_{r1} = 0$, eliminating the influence of E_{r1} and E_{r2}. The conditions for Figure 33 are the same as Figure 32 except $\gamma_{r2} - \gamma_{r1} = 180^\circ$. In this figure, it is clear that, the influence of E_{r1} and E_{r2} on F_{ta} is minimized as the value of L is increased. In fact when $L/L_{current} = 5$, the F_{ta} values are the same for $\gamma_{r2} - \gamma_{r1} = 0$ and $\gamma_{r2} - \gamma_{r1} = 180^\circ$ (in Figures 32 and 33). This indicates that a torsional shaft stiffness k_s value corresponding to $L/L_{current} = 5$ is sufficient to isolate the excitations created by the reaction gear pair from the test gear pair. Time histories $F_t(t)$ shown in Figure 34 for $L/L_{current} = 1, 3$ and 5 support this conclusion further.

Finally, the influence of shaft diameter d on the torsional natural frequencies ω_i is shown in Figure 35. Here ω_4 does not change significantly when $d/d_{current} \leq 1$. Meanwhile, increasing beyond $d_{current}$ does not improve on the resonance conditions as ω_2 is also brought near the operating speed range as well. In the process, the vibration isolation conditions are also worsened.

One other potential design change is to add inertias (flywheels) between the gear sets to further improve the dynamic isolation while moving the resonances away from the operation speed point. As the point of application of the flywheels become important, the 3D model is used here for this comparison. Figure 36 illustrates the 3D dynamic model of the NASA gear durability test rig with $L/L_{current} = 5$. In Figure 36(a), there is no added inertia while two inertias (one on each shaft) are included near the test gears in Figure 36(b). These flywheels are selected to have the same polar moments of inertia as the reaction gears, i.e. $J_{fi} = J_{ri} = 2.8 \times 10^{-3}\ kg - m^2$. In order to prevent any increase in the translational vibrations of the shafts, another set of bearings are mounted on the other side of the flywheels. In Figure 37, the resultant dynamic responses of these two configurations shown in Figure 36 are compared to that of the current system shown in Figure 20. Here, added shaft length alone is not sufficient to move the resonance peaks away from the operating speed of 10,000.

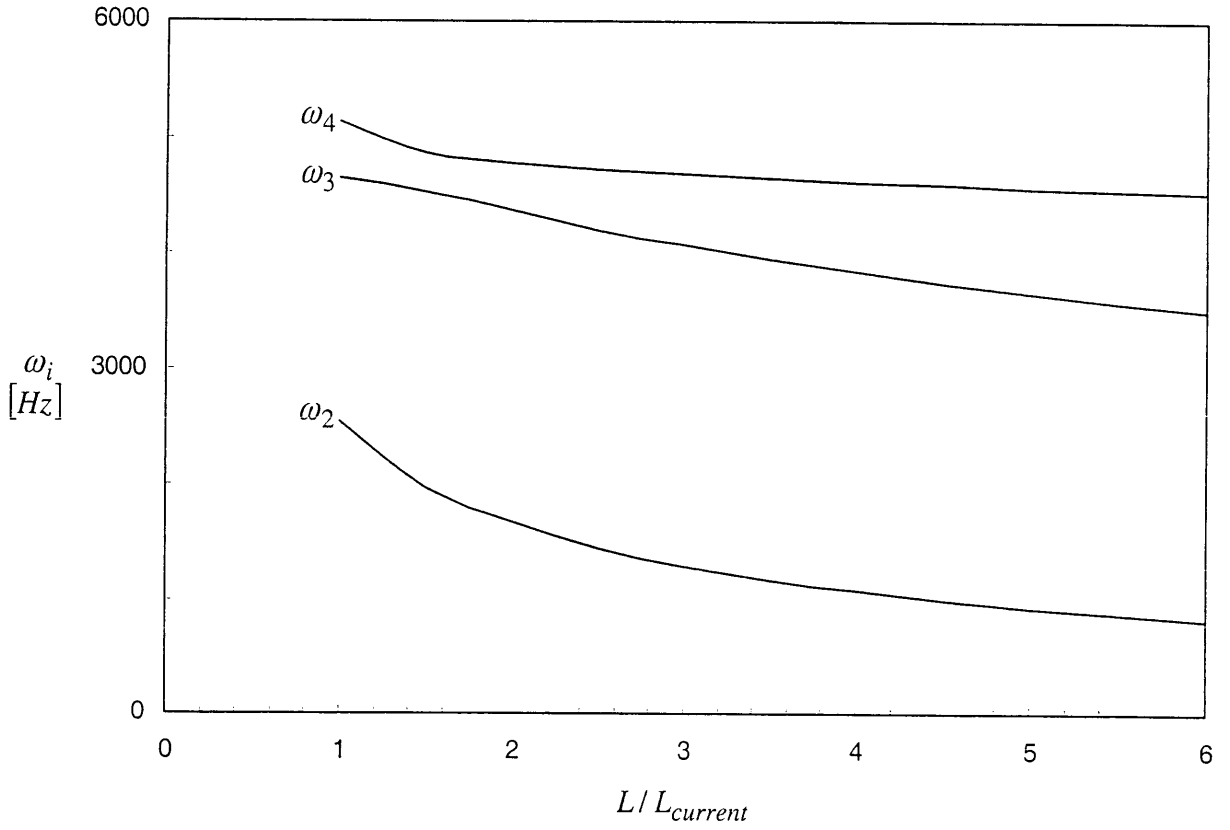

Figure 31 Influence of the length of the connecting shaft L on natural frequencies. $L_{current} = 112\ mm$ and $d_{current} = 34\ mm$.

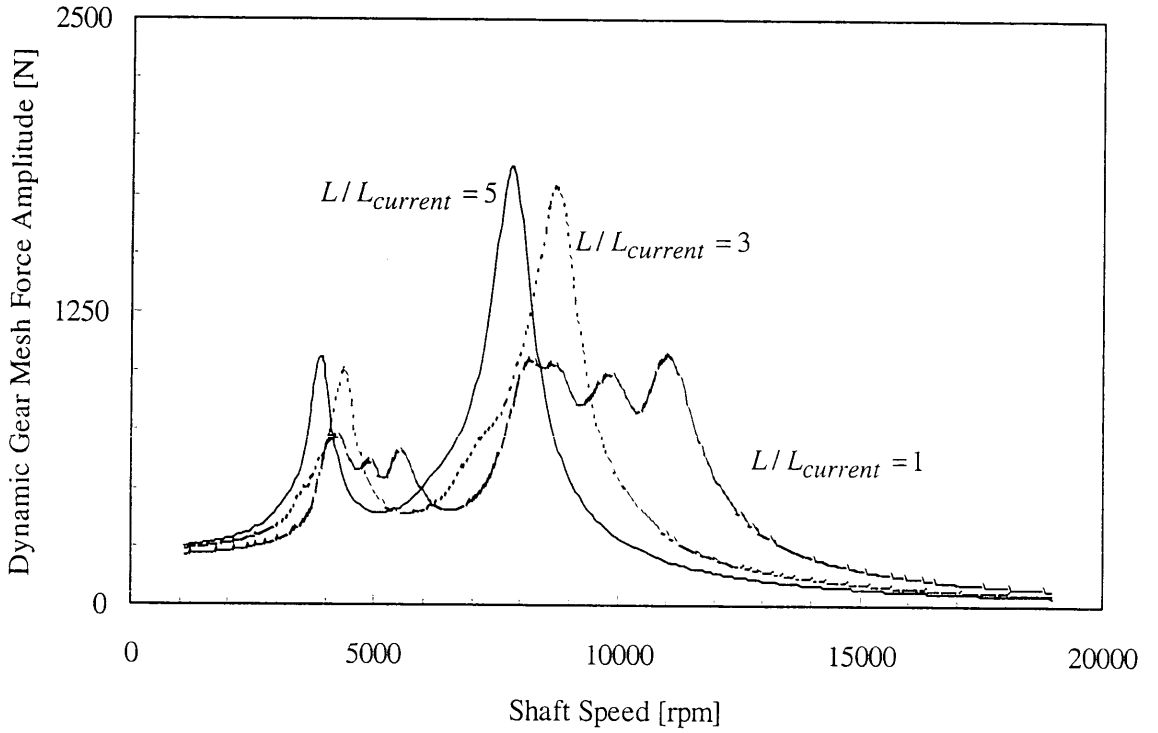

Figure 32. Influence of shaft length L on the dynamic force amplitude of the test gear pair with face offset. $\tilde{e}_{t1} = 2.26\,\mu m$, $\tilde{e}_{t2} = 1.11\,\mu m$, $\tilde{e}_{r1} = 0.67\,\mu m$, $\tilde{e}_{r2} = 0.42\,\mu m$, $E_{r1} = E_{r2} = 10\mu m$, $\gamma_{r1} = \gamma_{r2} = 0$, $L_{current} = 112\,mm$ and $d_{current} = 34\,mm$.

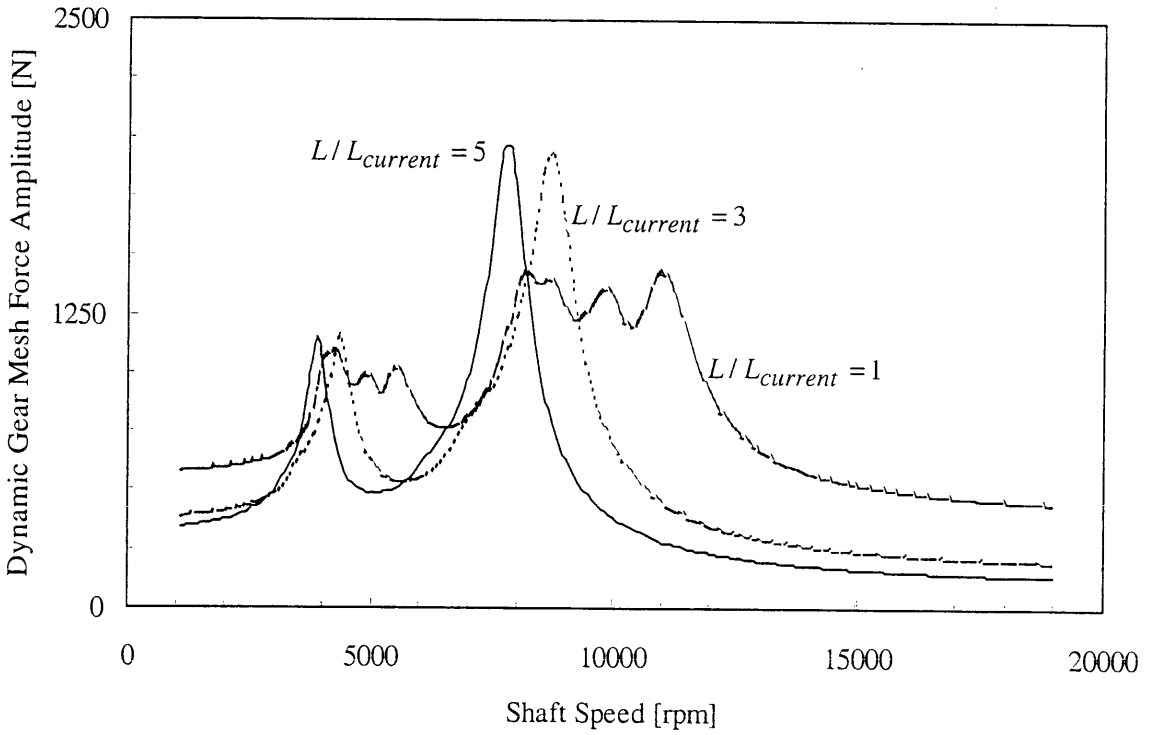

Figure 33. Influence of shaft length L on the dynamic force amplitude of the test gear pair with face offset. $\tilde{e}_{t1} = 2.26\,\mu m$, $\tilde{e}_{t2} = 1.11\,\mu m$, $\tilde{e}_{r1} = 0.67\,\mu m$, $\tilde{e}_{r2} = 0.42\,\mu m$, $E_{r1} = E_{r2} = 10\mu m$, $\gamma_{r1} = 0$, $\gamma_{r2} = \pi$, $L_{current} = 112\,mm$ and $d_{current} = 34\,mm$.

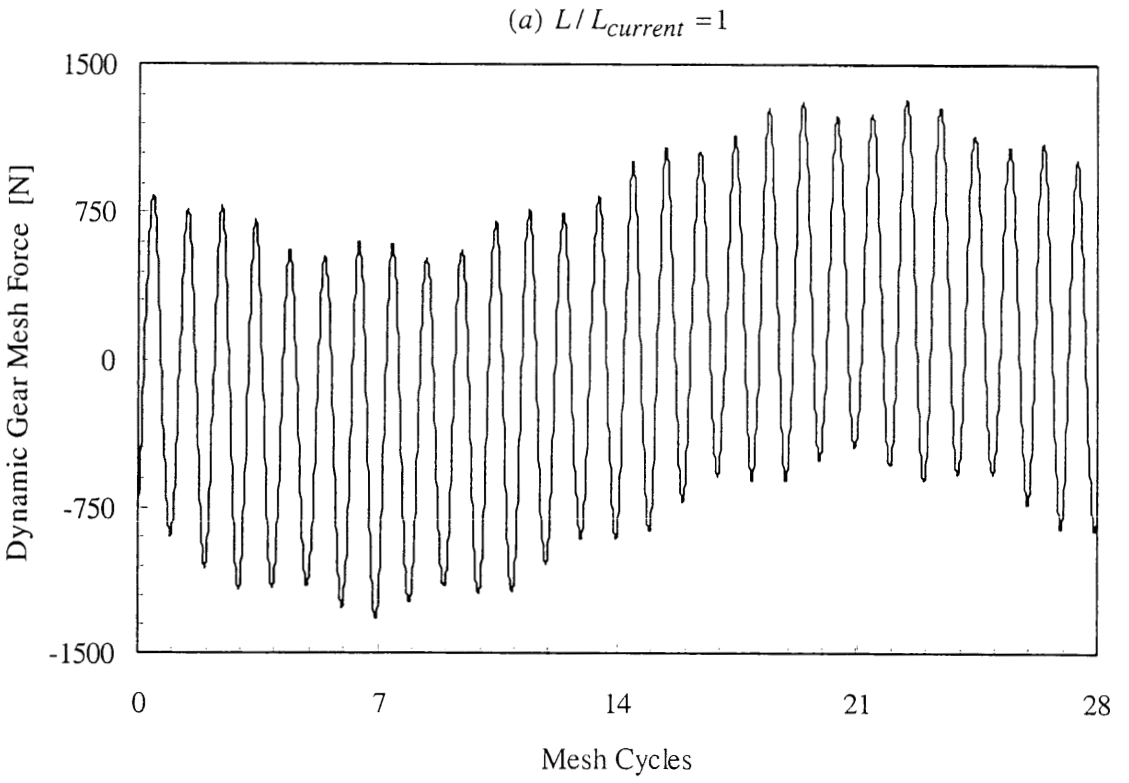

Figure 34. Dynamic force time history of the test gear pair with face offset at 10,000 *rpm* shaft speed. $\tilde{e}_{t1} = 2.26\,\mu m$, $\tilde{e}_{t2} = 1.11\,\mu m$, $\tilde{e}_{r1} = 0.67\,\mu m$ $\tilde{e}_{r2} = 0.42$, $E_{r1} = E_{r2} = 10\,\mu m$, $\gamma_{r1} = 0$ and $\gamma_{r2} = \pi$. (a) $L / L_{current} = 1$, (b) $L / L_{current} = 3$, and (c) $L / L_{current} = 5$

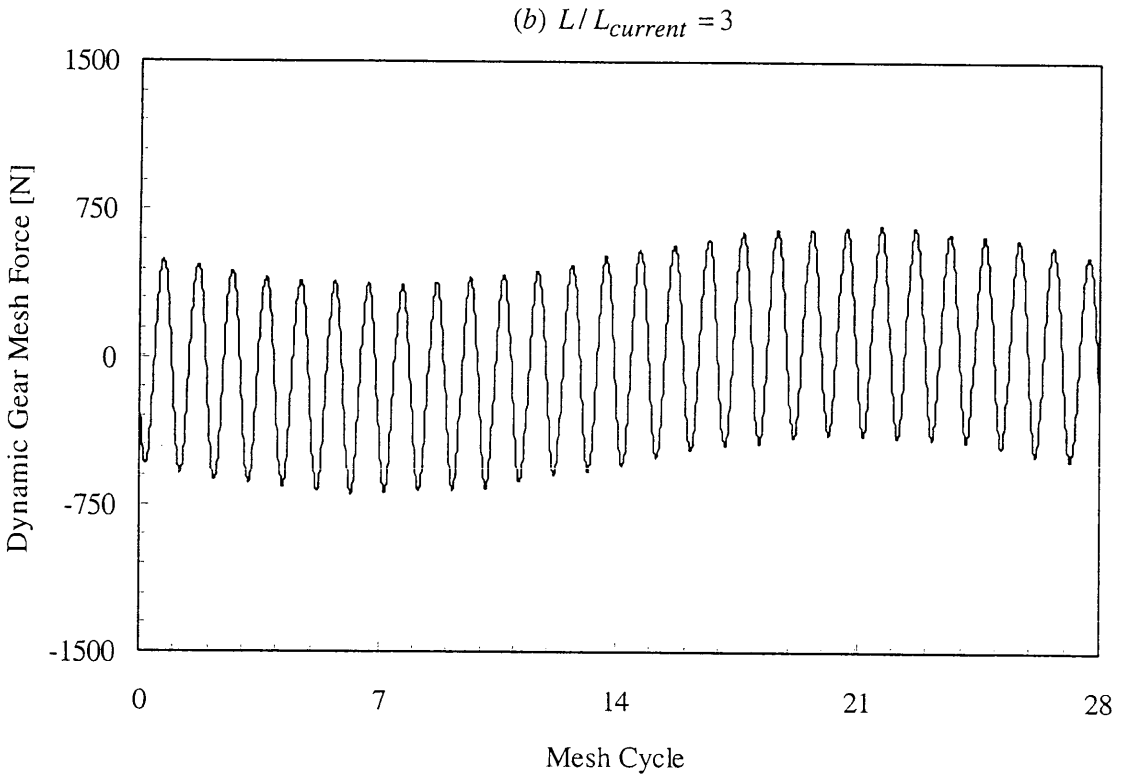

Figure 34. Continued.

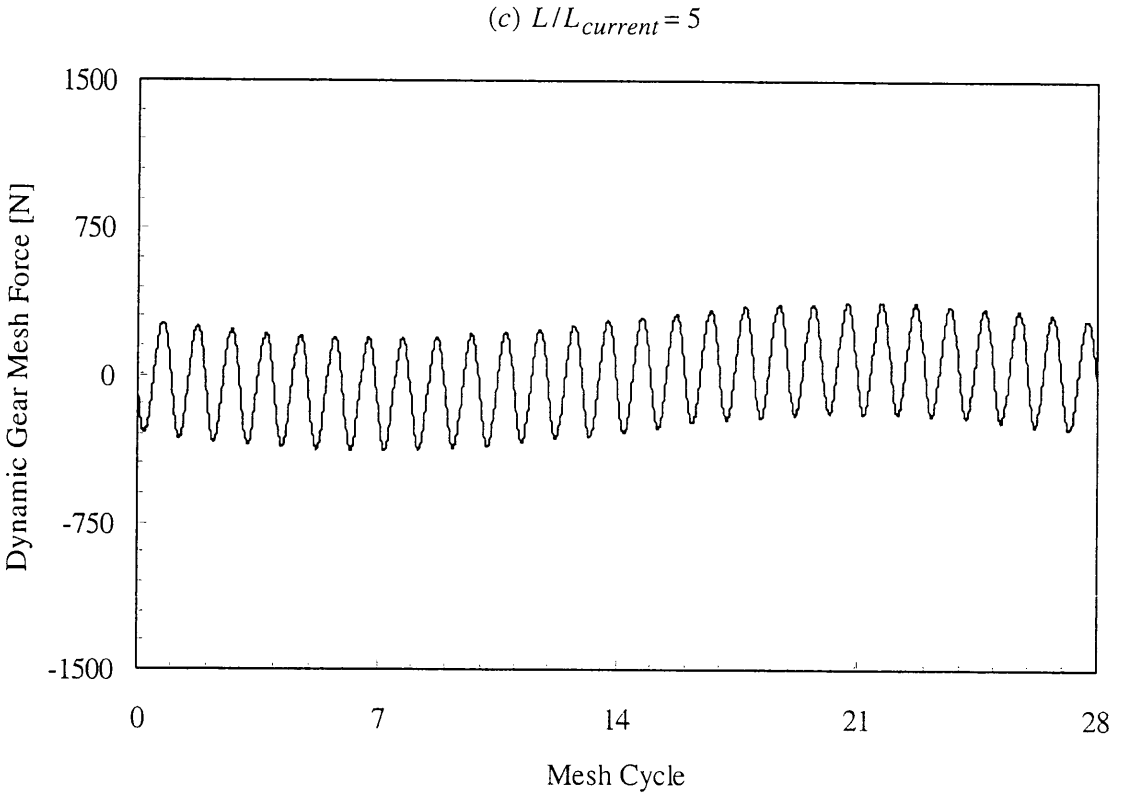

Figure 34. Continued.

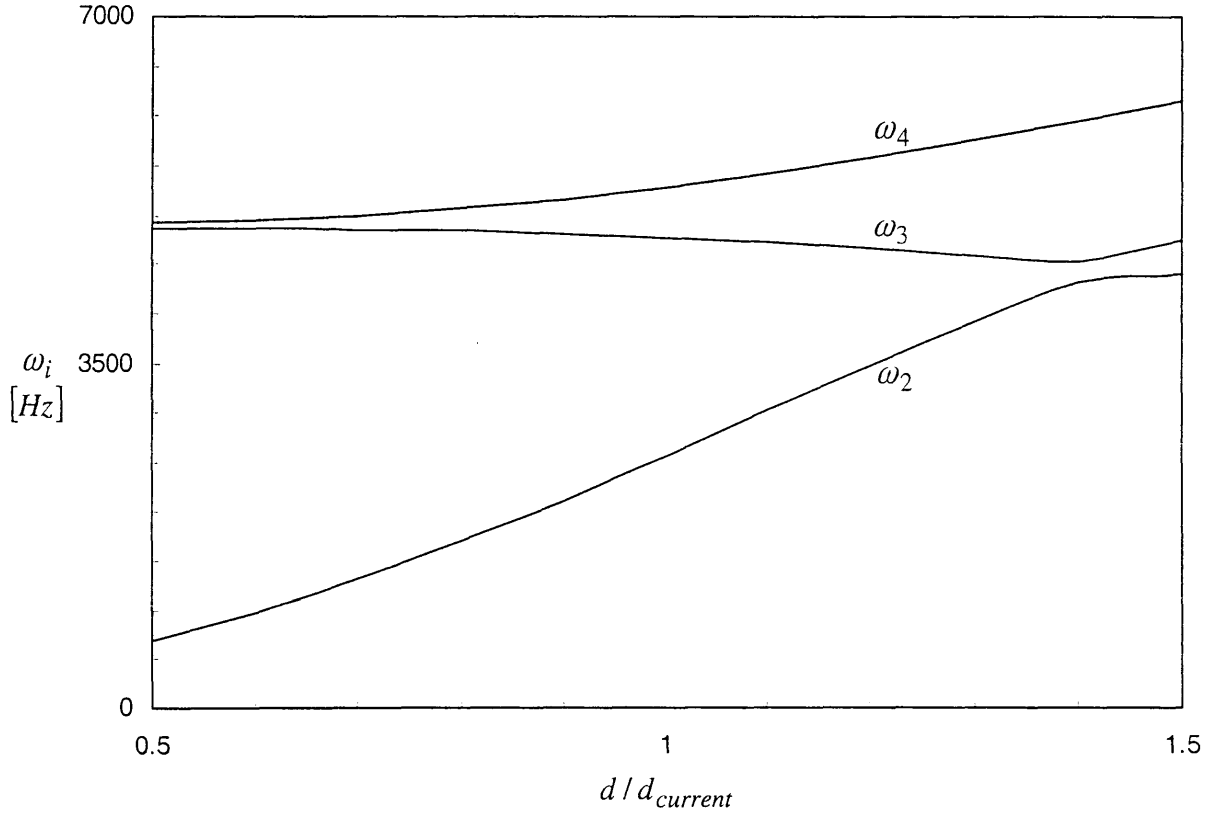

Figure 35. Influence of the diameter d of the connecting shaft on natural frequencies of torsional system. $L_{current} = 112\ mm$, $d_{current} = 34\ mm$.

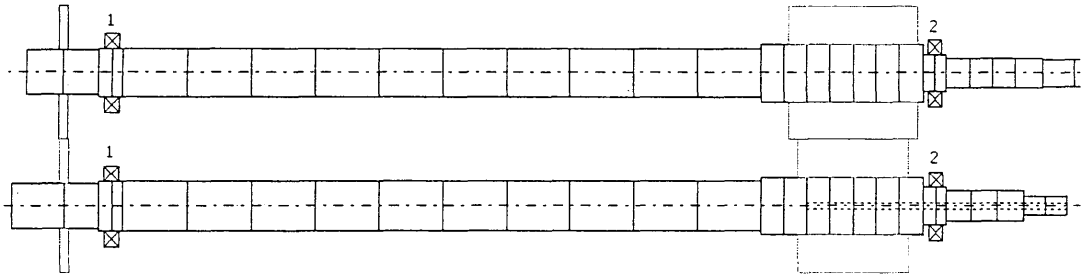

(a)

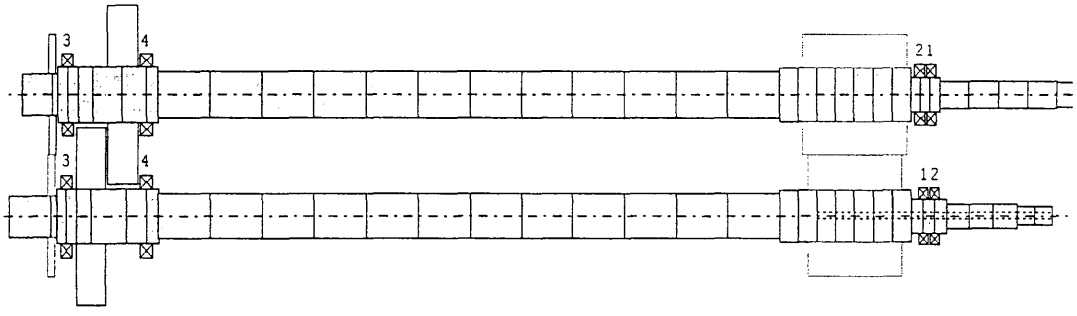

(b)

Figure 36. 3D Model of the test rig for $L/L_{current} = 5$;(a) without any additional inertias, and (b) with additional inertias near test gears.

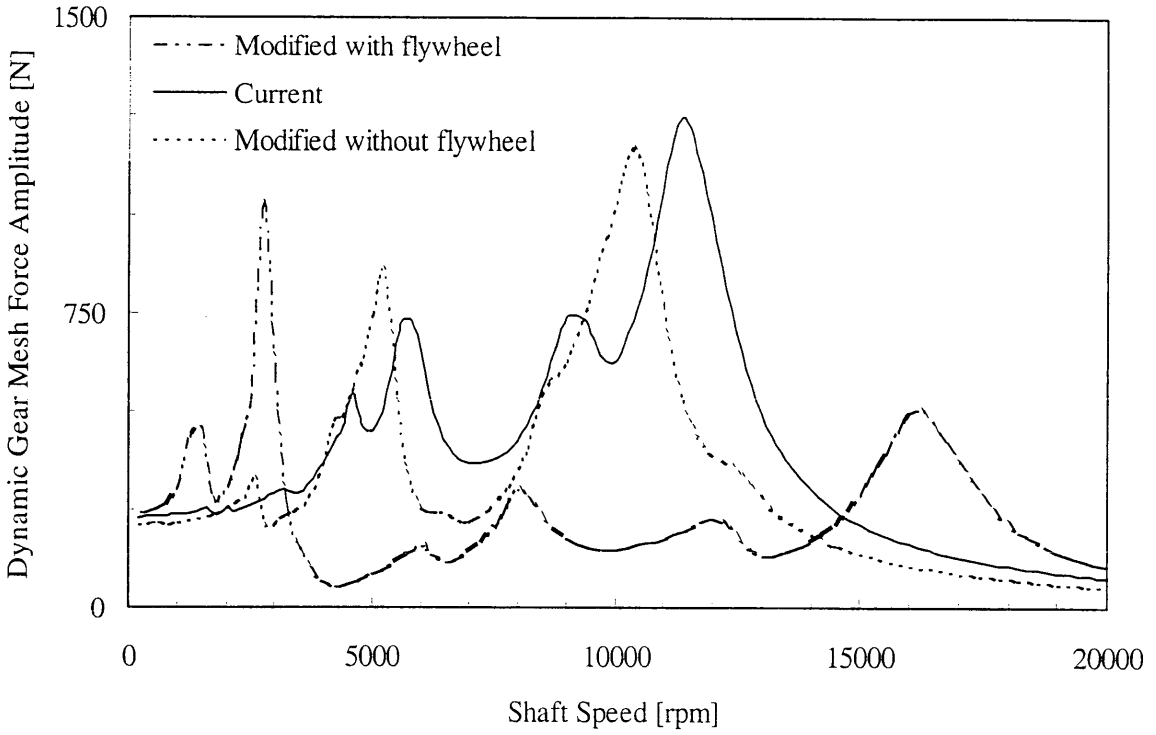

Figure 37. Comparison of the three configurations shown in Figures 20 and 36.

rpm. Meanwhile, the configuration shown in Figure 36(b) with added inertias eliminated most of the resonance peaks around 10,000 rpm. This suggests that a combination of added inertias and added compliance between the test and reaction gears can improve the resonance and vibration transmission characteristics of the test machine significantly

5. Conclusions

5.1 Summary

In this study, dynamic behavior of the NASA gear pitting machine is investigated. The current test and reaction gears are measured using a precision gear CMM and analyzed using a gear contact analysis model for describing their geometric and elastic properties and excitation mechanisms. Two different dynamic models, a purely torsional model and a three-dimensional model, were developed to predict the dynamic loads experienced by the gear meshes. The interactions of test and reaction gear pair were investigated. A number of potential design options were studied to quantify their impact on the dynamic and force isolation behavior.

5.2 Conclusions and Recommendations

Based on the results of this investigation, it can be concluded that the current test machine as operated at the current test conditions experiences dynamic loads that are due to the combined contributions of the excitations from both test and reaction gear sets. A number of resonance peaks exist near the operating test speed condition. The connecting shafts are too rigid to isolate any of the excitations from the reaction gear set from the test gear set. Accordingly, for the next-generation test machines, following changes to the current test rig are recommended:

- The overall flexibility of the shafts must be increased by changing the dimensions of the shafts. Results of this study indicates that at the current diameter, the distance between the test and reaction gear pairs should be at least five times the current dimension for an acceptable isolation of the reaction gear pair from the test gear pair. If the shafts to be maintained at the current length, torsionally flexible couplings can also be used for this purpose.

- Additional flywheels of certain amount of inertias can be implemented near the test gear pair to move the resonance peaks away from the operating speed condition resulting in a relatively resonance-free dynamic condition.
- An in-line torque meter should be incorporated to monitor loads experienced by the test gear set continuously.
- The face offset of the test gears should be eliminated and a slight lead crown should be incorporated in test gear design in order to improve the contact patterns and eliminate asymmetric (twisting type) tooth deflections that result in significant edge loading.
- The dynamic behavior of the new test rig layout must be studied using the dynamic models developed to prevent any undesirable conditions due to flexural motions of shafts and bearings.

For the future use of the current machine, following operational changes to the current test procedure can be recommended:

- The face offset of the test gears should be eliminated for the same reason as above.
- The reaction gears should be paired based on their indexing errors so that each have the same amount, if possible. In addition, they should be assembled in an "in-phase" condition for a cancellation of their influence on the transmission error excitation.

References

[1] Ewins, D. J., 1986, *Model Testing: Theory and Practice*, Research Studies Press, Hertfordshire, England.

[2] Kahraman, A., Ozguven, H. N., Houser, D. R., and Zakrajsek, J. J., 1992, "Dynamic Analysis of Geared Rotors by Finite Elements," *ASME Journal of Mechanical Design*, **114**, pp. 507-514.

[3] Kubur, M., 2002, *Dynamic Analysis of a Multi-shaft Helical Gear Transmission by Finite Elements*, M.S. Thesis, The University of Toledo, Toledo, OH.

[4] Ozguven, H. N. and Ozkan, Z. L., 1983, "Whirl Speeds and Unbalance Response of Multi-Bearing Rotors Using Finite Elements," *ASME Journal of Vibration, Acoustics, Stress, and Reliability in Design*, **106**, pp. 72-79.

[5] Kahraman, A., 1993, "Effect of Axial Vibrations on the Dynamics of a Helical Gear Pair," *ASME Journal of Vibration and Acoustics,* **115**, pp. 33-39.

[6] Lim, T. C. and Singh, R., 1990, "Vibration Transmission through Rolling Element Bearings, part I: Bearing Stiffness Formulation," *Journal of Sound and Vibration*, **139**, pp. 179-199.

[7] Krantz, T. L., Alanou, M. P., Evans, H. P., and Snidle, R. W., 2000, "Surface Fatigue Lives of Case-Carborized Gears with an Improved Surface Finish," Proceedings of ASME 2000 Design Engineering Technical Conference, DETC2000/PTG-14373.

[8] Townsend, D.P. and Shimki, J., 1994, "Evaluation of the EHL Film Thickness and Extreme Additives on the Gear Surface Fatigue Life,"AUSTRIB'94, Perth, Western Australia.

[9] Bajpai, P., 2002, *Development of a Surface Wear Model of Helical Gears*, M.S. Thesis, The University of Toledo, Toledo, OH.